# Facies and Diagenesis Distribution in an Aptian Pre-Salt Carbonate Reservoir of the Santos Basin Offshore Brazil: a Comprehensive Quantitative Approach

Ancilla Maria Almeida Carvalho, Youri Hamon, Olinto Gomes de Souza Jr, Nivea Goulart Carramal, Nathalie Collard

# Facies and diagenesis distribution in an Aptian Pre-Salt carbonate reservoir of the Santos Basin, offshore Brazil: a comprehensive quantitative approach.

**CARVALHO Ancilla Maria Almeida [1, 2], HAMON Youri [2], GOMES DE SOUZA Jr. Olinto [1], CARRAMAL Nivea Goulart [1], COLLARD Nathalie [2]**

(1) PETROBRAS, Av. Henrique Valadares, 28 – Centro, Rio de Janeiro-RJ, 20231-030, Brasil.

(2) IFP Energies Nouvelles, 1 et 4 Avenue de Bois-Préau, 92852 Rueil-Malmaison. France

*e-mail address of corresponding author: ancillacarvalho@petrobras.com.br

*Keywords:* Pre-salt, Santos Basin, Lacustrine carbonates, Diagenesis, Dolomitization

## Abstract

Aptian carbonate rocks of Santos Basin in the Brazilian southeastern continental margin show a highly heterogeneous reservoir quality conditioned by many controlling factors. This study presents a quantitative approach based on an integrated petrographic, mineralogical, and geochemical dataset of the Barra Velha Formation (BVF) to understand the spatial and temporal distribution of depositional and diagenetic aspects and the parameters controlling the nature and distribution of the diagenetic phases in Santos Basin pre-salt carbonate reservoirs. In this formation 3 units can be differentiated. The facies with higher Mg-clay content predominate in lower structural positions and regions with low relative relief. Higher proportions of spherulites occur in the transitional zones, and fascicular calcite occurs preferentially in the transitional and higher structural positions. Grainstones are observed in all depositional environments, but with variations in their composition (intraclasts, siliciclastic/volcanoclastic grain, and clay content). Stratigraphically, facies with higher Mg-clay content predominate in Units 3 (base) and 2 (intermediate), whereas Unit 1 (top) is marked by a greater proportion of grainstones and fascicular calcite. In Unit 1, fascicular calcite crusts tend to expand from the structural high, toward lower areas. The distribution of the main diagenetic products and their association with different facies highlight the role of depositional setting and primary constituents on the diagenetic processes. The tectonic and climatic context of the BVF favored the preferential precipitation and accumulations of Mg-clays in lower structural portions of the basin. The preservation of Mg-clays is also strongly linked to the structural setting, with more intense diagenetic alterations in higher structural areas. Dolomite is a major diagenetic phase in the studied samples, followed by silica. These diagenetic phases are largely associated with Mg-clay alteration and predominate in Unit 1. Mg-clays dissolution, as well as major alteration of carbonate phases, are concentrated in higher structural positions. Given the higher occurrence of faults in these areas and the presence of saddle dolomite, barite, celestine, and fluorite, which are typical products of hydrothermal alteration, part of the dissolution processes may be related to hydrothermal alteration. The depositional and diagenetic

aspects indicate a close connection between the hydrochemical evolution of the lake waters with the origin and diagenesis of these deposits.

## 1. Introduction

The Aptian Pre-salt carbonate section in the Brazilian Southeastern continental margin (Carminatti et al., 2009; Carlotto et al., 2017) represents a very unusual sedimentary system in terms of composition and dimension, raising questions about the environmental conditions that drove the sedimentation and early diagenetic evolution of these deposits (Terra et al., 2010; Wright, 2012; Herlinger et al., 2017). Given the occurrence of giant offshore reservoirs, this sedimentary formation has been recently widely studied, producing several conceptual models about its tectonic, stratigraphic, and sedimentological evolution (Karner and Gamboa, 2007; Lentini et al., 2010; Chaboureau et al., 2012; Mercedes-Martín et al., 2019; Minzoni et al., 2020).

These deposits were firstly interpreted as formed in a marine setting (Dias, 2005; Moreira et al., 2007; Gomes et al., 2009), then in an alkaline lacustrine environment (Wright, 2012; Muniz and Bosence, 2015; Tosca and Wright, 2015; Wright and Barnett, 2015; Herlinger et al., 2017; Tedeschi, 2017; Pietzsch et al., 2018; Tosca and Wright, 2018; Artagão, 2018; Lima and De Ros, 2019; Wright, 2022). Some of the first works analyzing the pre-salt deposits attributed their formation to microbial-influenced processes, referring to them as microbialites and stromatolites (Dias, 2005; Moreira et al., 2007; Terra et al., 2010, Muniz and Bosence, 2015; Mercedes-Martín et al., 2016), while others proposed an abiotic origin (Wright and Barnett, 2015; Tosca and Wright, 2015; Herlinger et al., 2017; Farias et al., 2019; Lima and De Ros, 2019; Gomes et al., 2020; Wright, 2022). These latter works reported the scarcity of macrostructures and microstructures characteristic of microbial carbonates, and the crystalline fabrics and isotopic composition indicative of an abiotic, chemogenic origin of the pre-salt deposits. Herlinger et al. (2017) interpreted these deposits as due to syngenetic precipitation

66 controlled by changes of the lacustrine geochemistry, resulting essentially in encrustation and
67 replacement of stevensite deposits.
68 The existence of peculiar features and mineral phases in these deposits allows the interpretation of
69 different precipitation conditions and makes it difficult to find an ideal analogue (Mercedes-Martín et
70 al., 2017; Deschamps et al., 2020; Magalhães et al., 2020; Wright, 2022). Furthermore, the close
71 connection between the syngenetic and eodiagenetic processes highlights the importance of
72 disentangling the diagenesis suffered by the pre-salt deposits (Herlinger et al, 2017, Lima and De Ros,
73 2019; Sartorato et al., 2020; Wright and Barnett, 2020). Several studies emphasised the role of early
74 diagenesis on the evolution of the deposits, mainly related to the dissolution of Mg-clay substrates and
75 its replacement by calcite spherulites, dolomite and silica (Tosca and Wright, 2015; Wright and Barnett,
76 2015, 2020; Herlinger et al., 2017; Farias et al., 2019; Lima and De Ros, 2019). In fact, the Aptian
77 carbonate rocks of Campos and Santos Basins show that reservoir quality is strongly conditioned by
78 the characteristics of the depositional environment and the associated diagenetic alterations (Rezende
79 and Pope, 2015; Herlinger et al., 2017). The impact of diagenesis on the evolution of porosity and
80 permeability is, according to several authors, not restricted to early alteration processes (clay
81 replacement or dissolution, calcite cementation), but also to the circulation of hydrothermal fluids in
82 some locations of the basin (Vieira de Luca et al., 2017; Lima and De Ros, 2019; Lima et al., 2020,
83 Sartorato et al., 2020).
84 Thus, the combination of these sedimentary and diagenetic processes leads to the formation of
85 complex and heterogeneous reservoirs. Understanding the spatial distribution of the diagenetic
86 products is essential to determine the factors controlling the reservoir properties and to be predictive
87 (Morad et al., 2012; Whitaker and Frazer, 2018). Although previous studies have provided detailed
88 petrographic analyses and paragenetic relationships of the primary and diagenetic constituents of the
89 Barra Velha Formation (BVF) from the Santos Basin (Wright and Barnett, 2015; Farias et al., 2019;
90 Wright and Barnett, 2020; Carramal et al., 2022) and the coeval Macabú Formation from the Campos
91 Basin (Herlinger et al., 2017; Lima and De Ros, 2019), an integrated quantitative view of the spatial and

temporal distribution of the syngenetic and diagenetic phases is lacking. The characterization and interpretation of these processes and products are still a matter of debate, and the definition of their quantitative distribution will contribute to the understanding of the paleoenvironmental conditions that drove the formation and modifications of these sediments.

Based on a huge database of petrographic descriptions, this study aims to present a comprehensive quantitative characterization of the main depositional and diagenetic features of the lacustrine carbonates of the Barra Velha Formation (BVF) from a key area of the outer high in the Santos Basin. It also seeks to present spatial and temporal distribution patterns of facies and diagenetic products at reservoir scale, based on petrography, mineralogical analyses and carbon and oxygen stable isotope data. Finally, it discusses the different processes (syngenetic, eodiagenetic and late hydrothermal-related) that control the reservoir heterogeneities of the South-Atlantic pre-salt succession. The results will contribute to a better understanding of the origin and evolution of these carbonate rocks and provide valuable constraints to reservoir characterization.

## 2. Geological Setting

### 2.1. Geodynamics

The Santos Basin, on the southeastern portion of the Brazilian continental margin, extends along the coast of Rio de Janeiro, São Paulo, Paraná e Santa Catarina states, between parallels 23° and 28° South, and covers a total area of approximately 350.000 $km^2$ (Figs. 1A and B). The basin is located between the Pelotas Basin to the south, bounded by the Florianopolis high, and Campos Basin to the north, bounded by the Cabo Frio high (Moreira et al., 2007).

The Santos Basin was formed during Early Cretaceous by the breakup of the Gondwana Continent. The Mesozoic rifting started in the southern parts of the South American continent in the Late Jurassic, reaching the equatorial margin by Late Aptian/Early Albian, culminating in the separation of South American and African Plates (Rabinowitz and LaBrecque, 1979; Conceição et al., 1988; Chang et al., 1992; Cainelli and Mohriak 1999; Moulin et al., 2010).

The South Atlantic Ocean can be divided into four long segments, from North to South: the Equatorial segment, the Central segment, the Austral Segment and the Falkland Segment. The beginning of the rupture, during the Jurassic, occurred in the southern portion of the Austral Segment (Popoff, 1988; Torsvik et al., 2009; Moulin et al., 2010). In the Equatorial segment, the movement of the continent to the north and northwest was impeded by the young oceanic lithosphere of the Central Atlantic Ocean, Gulf of Mexico, and proto-Caribbean (Szatmari and Milani, 2016). As a result, from about 145 to 113 Ma, the South Atlantic rift remained closed in the northwest, along the Equatorial margin, but widened wedge-like to the south, along the South America's eastern margin. As the rift widened, the basaltic volcanism along the Ponta Grossa and Namibia dike swarms created the proto-Walvis Ridge, which barred the access of ocean waters to the central South Atlantic rift from the South (Szatmari and Milani, 2016).

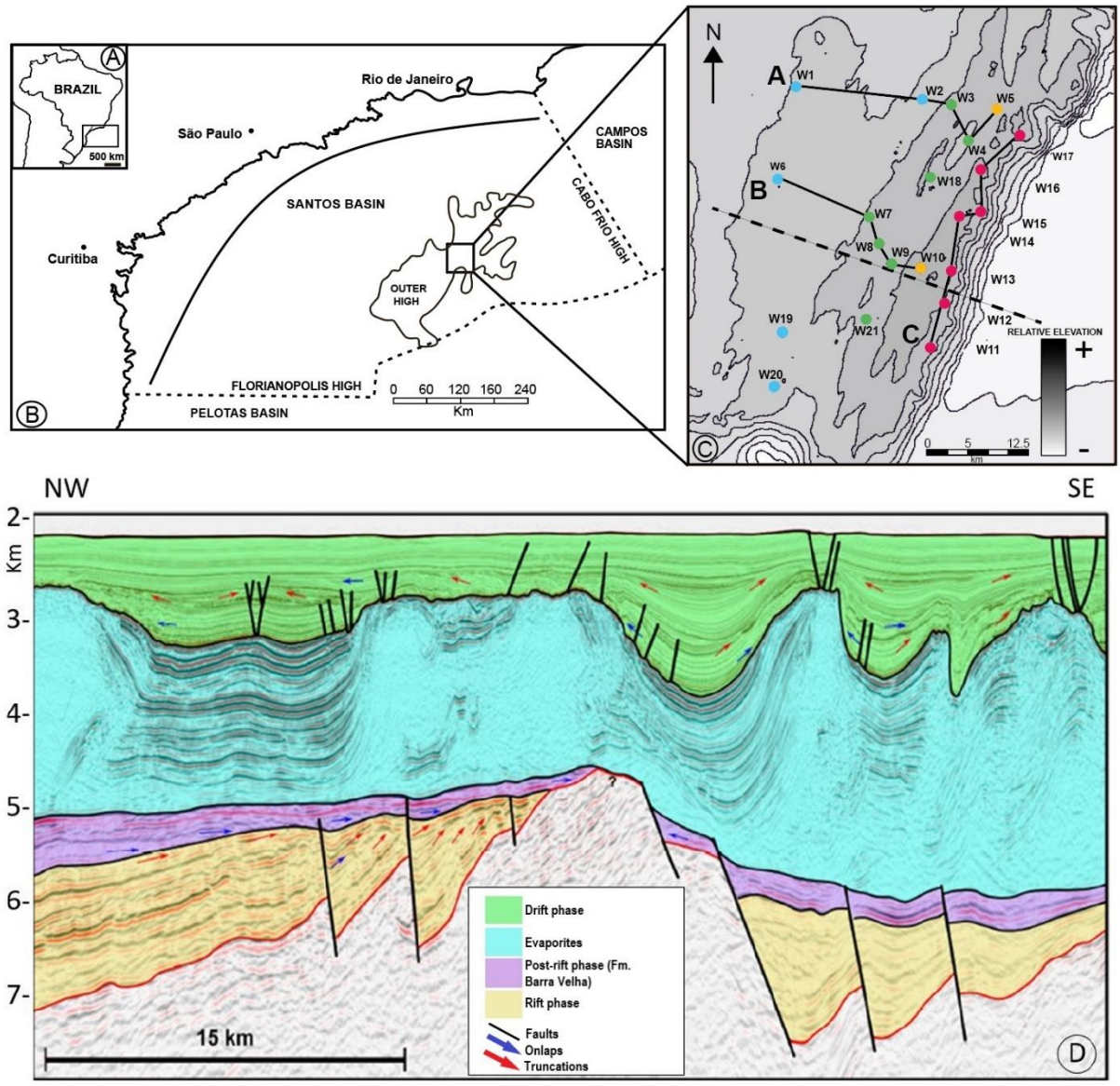


Figure 1 – A) Location of the Santos Basin in the southeast region of the Brazilian continental margin. B) Location of the study area in the middle of the outer high in the Santos Basin (modified from Papaterra, 2010 and Ysaccis et al., 2019). C) Structural map of the top of the Barra Velha Formation (base of the evaporitic section), showing the location of the wells (colored dots) in the study area. The colors refer to the four paleogeographic sectors distinguished in the study area: blue wells located in the lower part of the depositional profile, green wells located in the transitional area, orange wells located in the western part of the structural high, and pink wells located in the southeastern flank of the high. The dashed line represents the approximate location of the interpreted seismic line (D). D) Interpreted seismic section of the study area, southward to transect B, oriented perpendicularly to the topographic high and showing the different tectono-stratigraphic formations of the Santos Basin (modified from Artagão, 2018).

Moulin et al. (2010), reviewing the kinematics of the opening of the South Atlantic, proposed that from 132 to 130 Ma, the opening occurred between the Walvis Ridge and Pelotas Basin. After 130 Ma and until Aptian, the Santos block started to follow the general westward movement of the southern part of South America, playing the role of a kinematic buffer between the movements that created the northern Aptian basins. Since the rift was also barred from the Central Atlantic Ocean in the northwest, where the Equatorial margin had not yet rifted, an endorheic lacustrine basin formed (Szatmari and Milani, 2016).

Moreira et al. (2007) divided the tectono-stratigraphic evolution of Santos Basin into rift, post-rift and drift supersequences (Fig. 2). The basement of the Santos Basin is composed of Precambrian metamorphic rocks from the Mantiqueira Province, generated during the Neoproterozoic Brasiliano-Pan African Orogeny (Almeida et al., 1981; Heilbron et al., 2004).

The rift phase spans from Hauterivian to Early Aptian time (Pereira and Feijó, 1994), comprising the rocks of the Camboriú, Piçarras and Itapema Formations (Figs. 1D and 2). This phase is characterized by the development of rotated tilted-blocks and half-graben basins filled with thick sedimentary successions (Milani et al., 2007; Alves et al., 2017). The Piçarras Formation, deposited above the basaltic rocks of the Camboriú Formation, comprises alluvial sediments in proximal areas and shales of talc-stevensitic composition in lacustrine distal areas. In contrast, the Itapema Formation is composed of bivalve bioclastic rudstones concentrated on structural high domains, and of lime mudstones and organic-matter rich shales in the distal parts of the basin (Moreira et al., 2007).

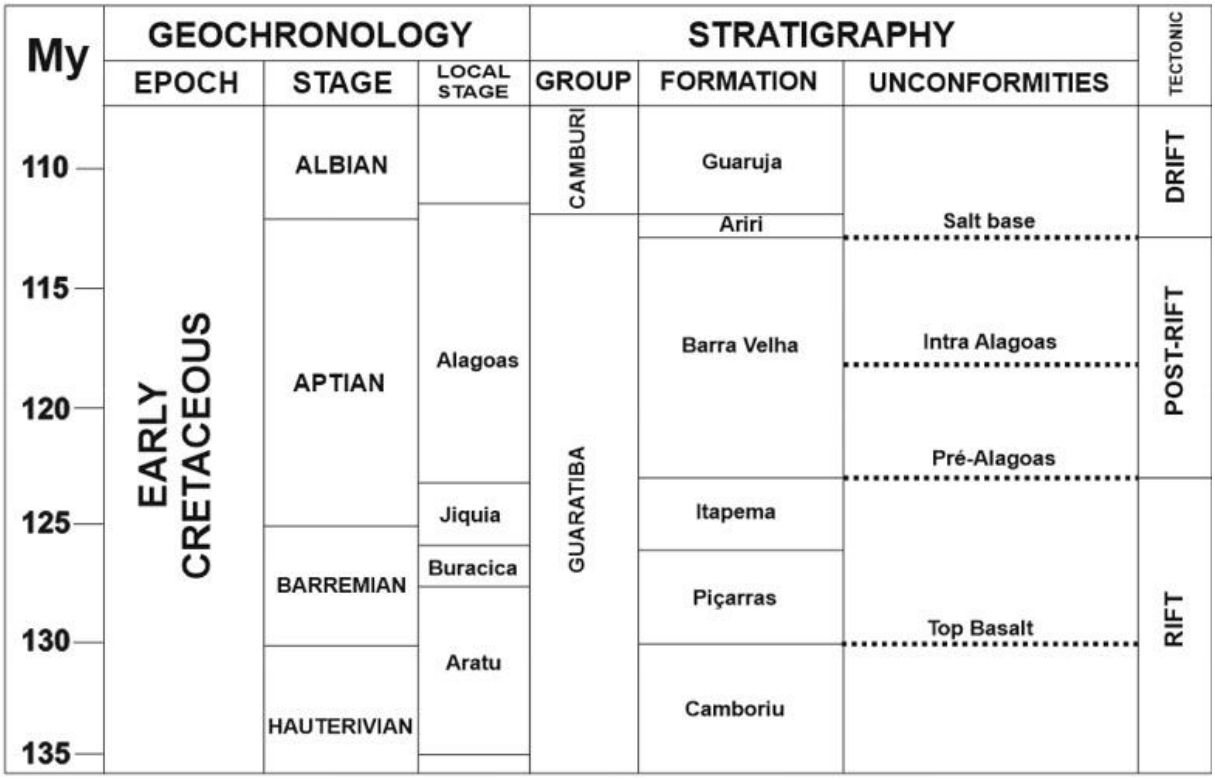


Figure 2 – Lower Cretaceous stratigraphic chart of the Santos Basin, Brazil (modified from Moreira et al., 2007).

From Barremian to Aptian, in the Central segment, the rift development is characterized by lithospheric extension, with block tilting in the inner upper continental crust and formation of small grabens occupied by lakes (Dias et al., 1988; Karner et al., 2003; Carminatti et al., 2008). A regional unconformity, related to uplift and erosion of the rift section (Winter et al., 2007; Moreira et al., 2007), the so-called Pre-Alagoas Unconformity, marks the transition to the Aptian post-rift phase (Fig. 2). The latest phase is characterized in the Santos Basin by the sediments of Barra Velha Formation (BVF), main topic of this article.

A phase of thermal subsidence followed, marked by an extensive deposition of evaporites during the uppermost Aptian and lowermost Albian (Muniz and Bosence, 2015; Gomes et al. 2020). The first marine ingressions promoted the deposition of halite and anhydrite in both South America and West Africa margins (Asmus and Ponte, 1973; Cainelli and Mohriak, 1999; Mio, 2005). With the progression

177 of the South Atlantic opening, the evaporites were overlain by an Albian marine carbonate platform,
178 corresponding with the passive margin phase of the basin (Chang et al., 1992, Mio, 2005).
179
180 2.2. Case study
181 The study area is situated in the central portion of the Santos Basin, on the outer high, with the wells
182 studied distributed over a 45 km x 56 km rectangular area (Fig. 1C). The base of the evaporitic section
183 (that overlies the BVF) is marked by structural lows and highs with NE-SW direction, reflecting the
184 paleotopography at the end of the BVF succession (Fig. 1C). The study region is characterized by a tilted
185 fault block delimitated by normal faults with SE dip; while the northwestern flank presents a ramp
186 morphology, with a low-angle slope, the SE region displays a steep faulted-flank (Fig. 1D). The sediment
187 thickness varies greatly towards the structural highs, where the basal part of the BVF can be absent
188 (Fig. 1D).
189 The BVF is bounded at the top by the evaporites of the Ariri Formation and at its base by the Pre-
190 Alagoas Unconformity. An internal unconformity called the Intra-Alagoas Unconformity separates the
191 post-rift phase into two stratigraphic units (Fig. 2). Previous stratigraphic and sedimentological studies
192 (Liechoscki de Paula Faria et al., 2017; Artagão, 2018; Gomes et al., 2020) allow the division of the BVF
193 into three stratigraphic units, informally named Unit 3 (base) to Unit 1 (top). The Intra-Alagoas
194 unconformity marks the top of Unit 3 (Fig. 2), whereas the stratigraphic surface that separates Units 2
195 and 1 is a major sequence boundary (Liechoscki de Paula Faria et al., 2017).
196 The BVF was initially interpreted as deposited in a transitional environment, from continental to
197 shallow marine settings (Moreira et al., 2007; Gomes et al., 2009). Later, several authors dismissed the
198 marine origin favoring the deposition of the BVF in an alkaline lacustrine environment (Wright, 2012;
199 Tosca and Wright, 2015; Wright and Barnett, 2015; Szatmari and Milani, 2016; Tedeschi, 2017; Pietzsch
200 et al., 2018). Based on petrographic descriptions from several wells of Santos Basin, Wright and Barnett
201 (2020) described the BVF as a highly heterogeneous combination of in-situ and re-worked grains, with
202 mineralogies comprising calcite, dolomite, magnesian silicates (stevensite and talc), and silica.

According to these authors, the dominant primary calcite components are fascicular crusts and spherulites, with some rare microbialites in the formation's uppermost 20–30 m. The carbonate components associated with Mg-silicate phases and the paucity of fish remains suggest highly restricted environments where mineral precipitation was dominantly controlled by the lacustrine water geochemistry (Herlinger et al., 2017; Mercedes-Martín et al., 2019; Wright and Barnett, 2020).

## 3. Material and methods

This work is based on data from 21 wells located at different positions within the study area and distributed on and from either side of a topographic, structural high (Fig. 1C). The use of “proximal” and “distal” terminology, to refer to positions relatively closer and away from the structural high seems inadequate as this terminology has a depositional significance, and criteria to confidently discriminate between both environments are unclear. The study area was thus divided into four sectors, allowing to delineate the distribution of sediments and diagenetic phases. The so-called higher area is represented by two wells, northwest of the structural high (W5 and W10). Seven wells are located on the southeastern steep flank (W11-W17). Six wells (W3, W4, W7, W8, W9, W18, and W21) are situated in the transitional area of the northwestern low-angle slope, whereas six other wells (W1, W2, W6,, W19, and W20) are located in the so-called lower area. The well data were also arranged in three transects (named Transects A, B, and C), either along or perpendicular to the structural high (Fig. 1C).
The database consists of core and petrographic descriptions (1483 thin sections), bulk-sample C and O isotopic analyses, quantitative evaluation of minerals by scanning electron microscopy and energy-dispersive X-ray spectroscopy (QEMSCAN) and X-ray diffraction (XRD) analyses, performed at Petrobras Research Center (CENPES) in Rio de Janeiro, Brazil.
The thin sections were prepared with blue epoxy resin impregnation and stained with alizarin red-S and potassium ferricyanide solution, to differentiate carbonate minerals (Dickson, 1965). Petrographic analyses were carried out with a Zeiss Imager A2 microscope, using both plane-polarized light (PPL)

and crossed-polarized light (XPL). A semi-quantitative visual estimation of primary and diagenetic constituents, and pore types, has been done using the comparison chart of Terry and Chilingar (1955). The petrographic analysis also focused on the description of texture, fabric and paragenetic relationships. The results were documented using the Petroledge© knowledge-based system. A statistical analysis was performed to evaluate the distribution and relationship between depositional and diagenetic phases.

Stable C- and O- isotope analyses of bulk rocks were performed on 503 samples, derived from core plugs and sidewall cores from 6 wells. For the analysis, a mass spectrometer Delta V Plus Advantage, coupled to a dispositive for extraction of $CO_2$ Kiel IV. 1 was used. The $^{18}O/^{16}O$ and $^{13}C/^{12}C$ ratios are expressed in the conventional 'δ' notation, in parts per thousand (‰), relative to Vienna Pee Dee Belemnite (VPDB).

Bulk-rock X-Ray Diffraction (XRD) analyses were obtained from 811 samples and clay fraction mineral composition analyses were performed for 503 samples. For the clay fraction analyses, the samples were fragmented using a Branson Cell Disruptor (Mod 350) and separated by several centrifuge steps. The identification of the clay minerals was performed on the air-dried samples, solvated with ethylene glycol, and subsequently heated at 490°C. The XRD analyses were performed in a RIGAKU D/MAX-2200/PC diffractometer. The identification of bulk mineralogy was determined using the Jade software (MDI) and the PDF-2 mineral database (ICDD). The quantitative analyses were performed using the Rietveld method (Young, 1993) with FullProf software (Rodriguez-Carvajal and Roisnel, 1998). Mineralogical maps of 92 samples from 5 wells were produced using the equipment QEMSCAN 650/FEI with two EDS/Bruker coupled detectors.

# 4. Results

## 4.1 Facies of the BVF

A vast body of literature dealing with the BVF in the Santos Basin exists today, with a relative consensus on its main components and textures, considered as a heterogeneous association of in-situ and re-worked constituents (Wright and Barnett, 2015; Herlinger et al., 2017; Tanaka et al., 2018; Farias et al., 2019; Basso et al., 2020; Gomes et al., 2020; Wright and Barnett, 2020). The in-situ facies components are fascicular calcite (shrubs), spherulites, microcrystalline calcite, and clay minerals, whereas the re-worked facies present different proportions of shrubs and spherulites intraclasts, siliciclastic/volcanoclastic grains, with variable clay content. Based on the relative contributions of each constituent, Gomes et al. (2020) proposed a consistent and rather exhaustive facies classification. However, to understand the large-scale sedimentary and diagenetic characteristics of the study area and simplify our data analysis, we have adopted the broader terminology of Lima and De Ros (2019). Thus, the major facies recognized in the BVF are fascicular calcite crusts (shrubs), Mg-claystones with spherulites, laminites, and intraclastic grainstones.

### 4.1.1 Fascicular calcite crusts (shrubs)

This facies consists of calcite crystals presenting fascicular-optical texture. These crystals grew predominantly in a vertical to sub-vertical orientation, with an average height of 2 mm (Fig. 3A). The crystal shrubs have a conical form in the longitudinal section that shows height greater than length (Farias et al., 2019), or in certain layers, incipient forms with a height/width ratio of about 1:1. The latter can be seen as morphologically intermediate forms between spherulites and crusts. The fascicular calcite crusts show intercalations with millimetric to centimetric layers of spherulites, re-worked particles (indistinct fragments of spherulites and shrubs), microcrystalline calcite, and dolomite, creating a laminated macroscopic aspect, with locally low relief domical forms. Each layered unit can reach 2 m in thickness.

279 The association with spherulites is frequent and can make up 30% of the samples. Minor constituents
280 comprise argillaceous peloids, ostracods bioclasts and Mg-clay laminations, which can be locally
281 incorporated into calcite aggregates (Fig. 3B). In 30 % of the samples, the Mg-clays appear as interstitial
282 sediment between the carbonate aggregates. The pore system is characterized by growth-framework
283 and inter-crystalline porosity types. The fascicular calcite crusts are not microporous.
284

285 **4.1.2 Mg-claystones with spherulites**

286 Mg-claystones are characterized by Mg-clays in association with different proportions of calcite
287 spherulites and dolomite (Figs. 3C-3E). For sake of clarity, the different clay minerals that constitute
288 these Mg-clays are characterized in part 4.3.2. The spherulites are spherical to sub-spherical calcite
289 crystal aggregates with a sweeping extinction and size generally less than 2 mm. It is possible to
290 categorize this facies into two distinct sub-facies, depending on the relative proportion of spherulites:
291 Mg-claystones with higher proportions of spherulites and Mg-claystones with minor proportions of
292 spherulites.
293 The Mg-claystones with higher proportions of spherulites (34% on average, 83% maximum) present
294 variable thickness, between 5 cm and 100 cm and display an irregular planar laminated structure,
295 marked by spherulites and clay laminae, showing a brownish color. The spherulites may occur
296 coalesced and recrystallized (Fig. 3C). The Mg-clays are present in 56 % of the samples and locally
297 represent 50 % of the sample constituents (Table 1). Silt- to sand-size siliciclastic grains of quartz and
298 muscovite are frequent and can occur as nuclei of the spherulites. Minor occurrences of ostracods are
299 also observed. The Mg-clays are commonly displaced by calcite spherulites (Fig. 3D) and frequently
300 show partial to total dissolution. The dissolution of the clay matrix and spherulites is the primary
301 process generating porosity in this facies, that initially possesses a low reservoir quality.

302 The Mg-claystones with minor proportions of spherulites exhibit a massive to layered structure (Fig.
303 3E), generally with centimetric bed thickness. Macroscopically it is characterized by centimetric
304 claystone layers and alternations of laminae with the sparse occurrence of spherulites. The spherulites

are observed in 30 % of the samples from this sub-facies, occurring as rare, isolated floating grains representing around 3% on average (10 % maximum) of the constituents. Samples without spherulites usually show intense dolomitization and replacement by microcrystalline calcite, resulting in the loss of the original fabric.

#### 4.1.4 Laminites

This facies is composed of alternating laminae of microcrystalline calcite, microcrystalline dolomite, Mg-clay, organic matter, and detrital components (quartz, feldspar, and micas). Macroscopically it is characterized by plane-parallel flat or crenulated laminations (Figs. 3F and 3G) and frequent organic-matter rich laminae. The colors vary between greenish and brownish, depending on the proportion of siliciclastic mud, carbonate, and Mg-clay content. Ostracods, phosphatic fragments and micro-spherulitic calcite are present in small quantities.

Fenestral and intercrystalline porosity are common across lamination. Microporosity is also frequent and given the remains of organic-matter rich laminae in some samples (Fig. 3H), the porosity generation could be related to organic matter degradation (Farias et al., 2019). The recrystallization of calcite crystals is frequently observed, and occasional breccia and teepee structures occur, associated with the crenulated laminites (Fig. 3I). The breccia is poorly sorted, made up of millimetric to centimetric, subangular intraclasts of laminites, in a matrix of microcrystalline dolomite. Some of the intraclasts are dolomitized and silicified.

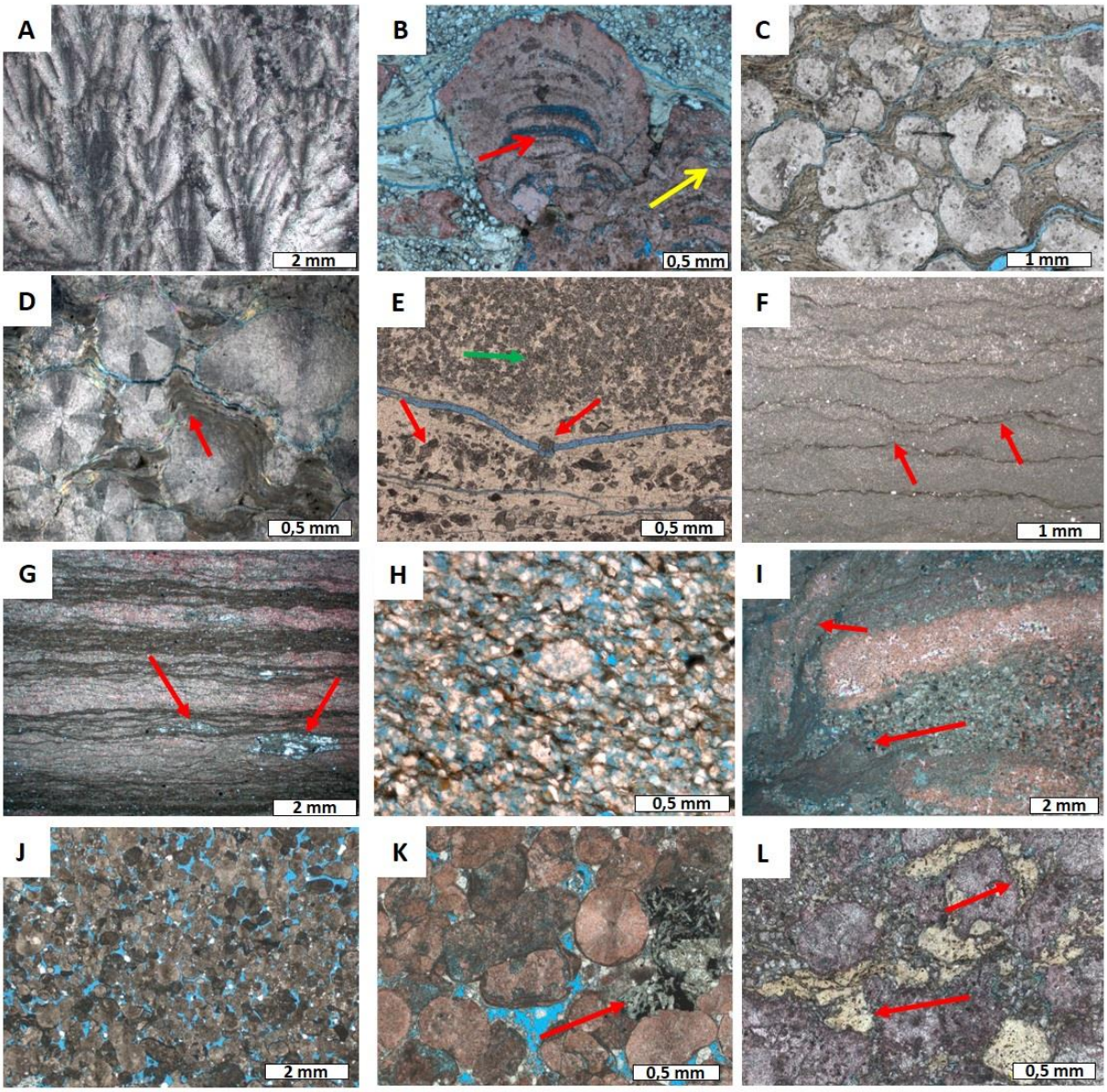


Figure 3 – Photomicrographs highlighting main facies of the Barra Velha Formation: (A) Fascicular calcite crusts (crossed-polarized light; XPL); (B) Mg-clay matrix engulfed by shrubs (yellow arrow). Note the shrubs partially dissolved (red arrow) (plane-polarized light; PPL);16; (C) Mg-claystones with spherulites, showing coalesced and recrystallized spherulites (PPL); (D) Mg-claystones with spherulites showing a displacement aspect of the Mg-clay (red arrow) (XPL); (E) Mg-claystone with very fine dolomite crystals (green arrow) and dolomite rhombs (red arrows). Note the absence of spherulites in this sub-facies (PPL); (F) Laminites composed by microcrystalline calcite. Red arrows highlight dissolution seams (PPL); (G) Laminites with a crenulated morphology, composed by intercalations of very fine calcite crystals, dolomite, and organic matter. Red arrows highlight millimeter-scale silica nodules (XPL); (H) General aspects of organic matter remnants (PPL); (I) General aspects of breccia features in laminites. Red arrows highlight the intraclasts (XPL); (J) Intraclastic grainstone (Type-A) composed by fragments of fascicular calcite crusts and spherulites (PPL); (K) Type-B grainstone with volcanoclastic fragments (red arrow) (PPL); (L) Type-C grainstone (packstone) composed of carbonate and Mg-clay intraclasts (red arrows), with a minor fraction of siliciclastic grains (PPL).

Table 1 – Statistical summary of the average and maximum amounts of major constituents, Mg-clay and secondary porosity, in the main facies of the Barra Velha Formation. GST= intraclastic grainstones, SHR= fascicular calcite crusts, SPH= Mg-claystones with higher spherulites content, MGC= Mg-claystones with lower spherulites content, LAM= laminites.

| Lithologic types | | GST | | SHR | | SPH | | MGC | | LAM | |
|---|---|---|---|---|---|---|---|---|---|---|---|
| Constituents (%) | | Average | Maximum | Average | Maximum | Average | Maximum | Average | Maximum | Average | Maximum |
| Calcite | Fascicular crusts | - | - | 45.00 | 90.00 | 3.00 | 30.00 | 0.10 | 4.00 | 1.20 | 22.00 |
| | Spherulites | - | - | 6.50 | 32.00 | 34.00 | 83.00 | 3.00 | 10.00 | 1.60 | 33.00 |
| | Other Diagenetic phases | | | | | | | | | | |
| Mg-clay | Syngenetic | 1.00 | 38.00 | 2.00 | 30.00 | 5.00 | 50.00 | 14.00 | 83.00 | 3.00 | 35.00 |
| Calcite | Replacing constituents | 0.06 | 5.00 | 3.30 | 70.00 | 4.31 | 56.00 | 20.4 | 71.5 | 18.5 | 90.5 |
| | Filling primary porosity | 4.58 | 34.00 | 2.61 | 34.00 | 0.7 | 52.00 | 2.04 | 50.00 | 1.24 | 67.00 |
| | Filling secondary dissolution porosity | 0.04 | 3.00 | 0.5 | 25.00 | 0.34 | 8.00 | 0.03 | 1.00 | 0.27 | 10.00 |
| | Filling fracture porosity | 0.01 | 1.00 | 0.21 | 8.00 | 0.02 | 2.00 | 0.17 | 5.00 | - | - |
| Dolomite | Replacing constituents | 7.34 | 93.00 | 9.18 | 61.00 | 24.5 | 86.00 | 27.00 | 86.5 | 27.00 | 83.00 |
| | Filling primary porosity | 6.78 | 54.00 | 4.66 | 63.00 | 1.04 | 51.00 | 1.31 | 35.5 | 1.67 | 40.00 |
| | Filling secondary dissolution porosity | 0.15 | 29.5 | 0.71 | 35.00 | 0.94 | 25.00 | 0.32 | 7.00 | 1.00 | 35.00 |
| | Filling fracture porosity | 0.001 | 1.00 | - | - | 0.01 | 5.00 | 0.02 | 2.00 | 0.005 | 0.5 |
| Quartz | Replacing constituents | 2.68 | 70.00 | 4.25 | 65.00 | 5.65 | 97.00 | 6.71 | 55.00 | 8.91 | 72.00 |
| | Filling primary porosity | 2.08 | 53.00 | 1.73 | 58.00 | 0.62 | 33.00 | 0.39 | 15.00 | 0.32 | 10.00 |
| | Filling secondary dissolution porosity | 0.09 | 11.00 | 0.63 | 18.00 | 0.44 | 16.00 | 0.31 | 5.00 | 0.24 | 5.00 |
| | Filling fracture porosity | 0.01 | 2.00 | 0.09 | 8.00 | 0.03 | 10.00 | 0.08 | 6.00 | 0.07 | 3.00 |
| Baryte | Replacing constituents/Filling porosity | 0.07 | 5.00 | 0.08 | 5.00 | 0.05 | 4.00 | 0.13 | 0.47 | 0.03 | 2.00 |
| Celestite | Replacing constituents/Filling porosity | 0.004 | 2.00 | - | - | - | - | - | - | 0.01 | 2.00 |
| Chalcedony | Replacing constituents/Filling porosity | 0.35 | 17.00 | 0.78 | 30.00 | 1.15 | 80.00 | 0.4 | 10 | 2.1 | 45.00 |
| Cryolite | Replacing constituents/Filling porosity | 0.01 | 11.00 | 0.01 | 3.00 | 0.00 | 5.00 | - | - | 0.02 | 3.00 |
| Dawsonite | Replacing constituents/Filling porosity | 0.17 | 7.00 | 0.22 | 8.00 | 0.24 | 6.00 | 0.11 | 3.00 | 0.08 | 3.00 |
| Fluorite | Replacing constituents/Filling porosity | 0.002 | 1.00 | - | - | - | - | - | - | 0.03 | 5.00 |
| Illite/smectite | Replacing constituents/Filling porosity | 0.001 | 1.00 | - | - | 0.02 | 5.00 | - | - | - | - |
| Kaolinite | Replacing constituents/Filling porosity | 0.001 | 3.00 | 0.001 | 3.00 | 0.02 | 3.00 | 0.47 | 0.13 | - | - |
| Magnesite | Replacing constituents/Filling porosity | 0.15 | 15.00 | 0.73 | 27.00 | 1.59 | 46.00 | 0.42 | 22.00 | 0.8 | 25.00 |
| Secondary dissolution porosity | | 5.00 | 31.00 | 5.00 | 40.00 | 5.00 | 24.00 | 2.00 | 25.00 | 4.00 | 30.00 |

### 4.1.5 Intraclastic grainstones

The intraclastic grainstones are the main facies in the study area, representing 44 % of the available samples. They are composed predominantly of fragments of fascicular calcite crusts, spherulites, laminites, and different proportions of siliciclastic/volcanoclastic grains and Mg-clay intraclasts (Fig. 3J-3L). The carbonate intraclasts are commonly rounded, moderately to well-sorted, with size ranging between fine- and coarse-sand (locally very coarse), with tangential to long grain contacts (Taylor, 1950). Sutured and concave-convex contacts are observed but other compaction features (fractures, stylolithes, solution seams) are rare. This facies has a predominantly massive aspect but may present

a normal grading and cross-stratification. Intercalations with centimetre-thick layers of laminites and fascicular calcite crusts are frequent.

The association of the different components allows to categorise the grainstones in three different sub-facies, depending on the proportion of these components. Type-A grainstones are dominated by carbonate fragments, with low content or absence of Mg-clays and siliciclastic/volcanoclastic grains. They are the most common type (Fig. 3J). Type-B grainstones, composed of the most significant content of siliciclastic/volcanoclastic grains, generally contain silt-sized detrital constituents (quartz, feldspar, and mica) and sub-rounded to sub-angular basaltic volcanoclastic fragments (Fig. 3K). They display inverse grading and concavo-convex to sutured grain contacts. Finally, type-C grainstones range between a packstone to grainstone texture. They show the most prominent content of Mg-clays (both as grains or matrix) and are characterized by the presence of ooids, peloids and clay intraclasts (Fig. 3L). The Mg-clay content can be partially to totally replaced by calcite. They also show minor amounts of ostracods, phosphatic fragments, siliciclastic grains, and volcanoclastic rock fragments.

### 4.2 Facies distribution

The well dataset enables the construction of correlation transects, which can help to define the facies distribution and proportions, both in a spatial and temporal point of view (Fig. 4). These profiles were reconstructed based on the basement topography assessed from seismic interpretation (Artagão, 2018). In the same way, schematic fault proportions are located on these profiles to represent a simplified scheme of the fault network. These profiles show the existence of a topographic structural high (wells W5 and W10), with a southeastern steep flank (wells W11 to W17) and a northwestern low-angle slope (W1 to W4 and W6 to W9).

From a spatial point of view, the facies with a large Mg-clay content (grainstones with Mg-clays and Mg-claystones with minor proportions of spherulites) predominate in lower areas, away from the structural high, and in relatively low areas within the structural high, as in the case of well W4 (Fig. 4). Furthermore, the wells situated in higher structural positions show very low preservation of the Mg-

clays, which occurs mainly as ooids and peloids, intensively affected by diagenetic processes (as previously reported by Carramal et al., 2022).

The Mg-claystones with high proportions of spherulites predominate in lower and transitional areas and fascicular calcite crusts occur preferentially in the transitional areas and some locations of the structural high (Fig. 4). Minor occurrences of spherulites and incipient forms of shrubs with Mg-clays are also observed in lower areas of the depositional profiles. In the studied wells, the proportion of laminites is generally scarce and preferentially distributed in the transitional areas, with minor occurrences in the lower areas. However, crenulated laminites occur in Unit 1 of BVF, and mostly on the structural highs. The grainstones are observed along the entire transects, but with variations depending on the grainstone sub-facies. The carbonate intraclastic grainstones occur preferentially on the structural highs, whereas the grainstones with the largest content of Mg-clay are more developed in the lower areas. Finally, the siliciclastic/volcanoclastic-dominated grainstones occur mainly in Units 3 and 2, preferentially on the structural highs.

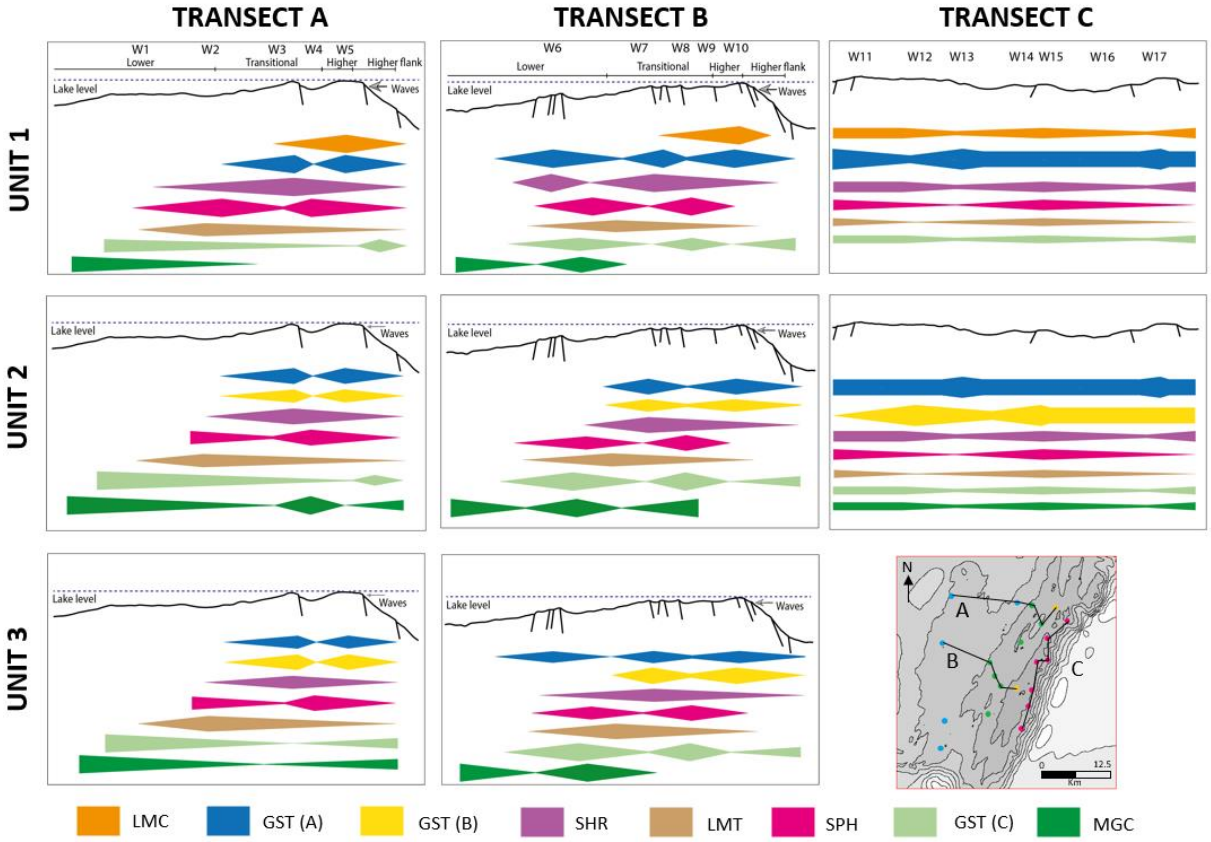

Figure 4 – Facies spatial and stratigraphic distribution over the three transects (A to C, located on the map of the study area) and the three stratigraphic units labeled 3 (base) to 1 (top). No interpretation was proposed for Unit 3 of transect C, as this unit pinches out on the basement. The scale of these transects is given on the map. LMC= crenulated laminites, GST (A)= intraclastic grainstones, GST (B) intraclastic grainstone with siliciclastic/volcanoclastic content, SHR= fascicular calcite crusts, LMT= laminites, SPH= Mg-claystones with higher spherulites content, GST (C) intraclastic grainstones with Mg-clay content, MGC= Mg-claystones with lower spherulites content.

Regarding the stratigraphic distribution, the most significant proportions of Mg-claystones with minor proportions of spherulites occur in Units 3 and 2. The Mg-claystones with high amount of spherulites predominates in Unit 1. Fascicular calcite crusts and intraclastic grainstones predominate in Unit 1. The latter is marked by a more significant proportion of fascicular calcite crusts, particularly towards the lower area of transect B. Some sites of the southeast flank show a high proportion of fascicular calcite crusts in Unit 3, as in the case of well W11. Detrital content, mainly associated with laminites, Mg-claystones with spherulites, and grainstones, generally occurs in low quantities. However, its abundance shows a progressive decrease from Unit 3 to Unit 1 (Table 2). A slight decrease is observed on the structural high (Table 3).

## 4.3 Facies and clay mineralogy

### 4.3.1 QEMSCAN analysis

The mineralogical composition of 92 samples from 5 wells located in different structural positions has been mapped using the QEMSCAN system. The samples consist mainly of calcite, dolomite, quartz, and Mg-clays, the latter varying significantly in proportion depending on the well position in the study area, reaching a maximum of 50 % in distal wells. The sum of the trace minerals represents average quantities of 3 % and the most common are presented in Figure 5.

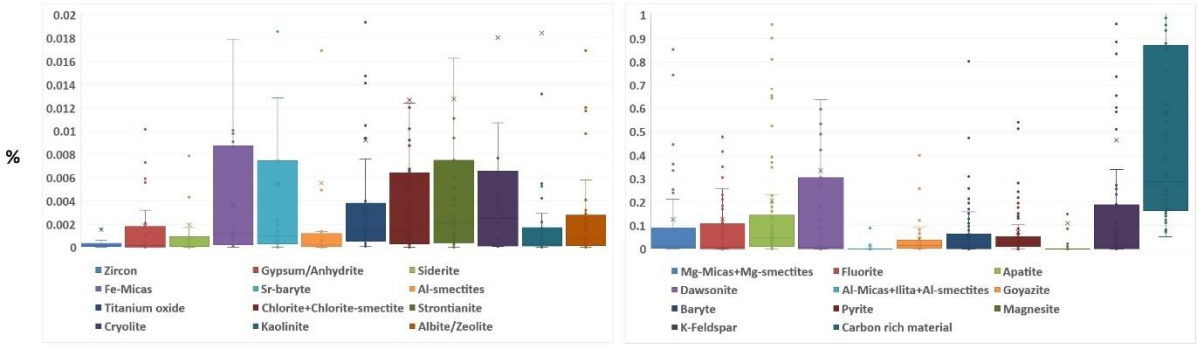


Figure 5 – Boxplots showing the diversity and amounts of accessory minerals encountered in the Barra Velha Formation, based on QEMSCAN analyses. A) Proportions of trace minerals. B) Proportions of minor minerals.

### 4.3.2 XRD analysis

Clay minerals occur in different proportions in the described facies, but also with different mineralogy. Bulk-rock X-Ray Diffraction (XRD) analyses show that the sum of calcite, dolomite, quartz, and clay minerals represent 90 % of the sample's composition. Among the secondary minerals Ca-dolomite, K-feldspar, and magnesite are the most representative. The larger and more complete sample dataset analyzed with XRD may explain some differences with the QEMSCAN analyses.

According to the XRD analyses, the clay minerals are composed chiefly of kerolite, mixed-layer kerolite/Mg-smectite, Mg-smectite, sepiolite, and minor amounts of non-magnesian clay minerals, such as Illite, illite–smectite, kaolinite and chlorite (Fig. 6A and 6B). Mg-smectite comprised stevensite and saponite (Netto et al., 2022) but their differentiation implies additional analyses that were not done for our dataset. Figure 6B shows the association between facies and the different clay species.

Kerolite and mixed-layer kerolite/Mg-smectite are the main Mg-clays observed in the case study (Fig. 6A and 6B). The analyses show that kerolite and mixed-layer kerolite/Mg-smectite are present respectively in 73 % and 55 % of the Mg-claystones with high amounts of spherulites (Supplementary material Fig. A1). In the intraclastic grainstones, kerolite occurs in 82 % of the analyzed samples, whereas mixed-layer kerolite/Mg-smectite is only present in 50 % of the samples. Kerolite occurs in 70 % of the fascicular calcite crusts, whereas mixed-layer kerolite/Mg-smectite is present in 40 % of the samples. Kerolite is also present in 67 % of the samples of laminites facies, but in low proportions (1-

10 % of each sample), whereas the mixed-layer kerolite/Mg-smectite represents more than 50 % of the clay fraction in 44 % of the samples.

Mg-smectites occur mostly related to intraclastic grainstones and fascicular calcite crusts, being present in 20 % of the samples and in those cases representing more than 50 % of the clay fraction (Fig. 6B). Sepiolite is rare, being present preferentially in fascicular calcite crusts (where it is present in less than 10 % of the samples and representing 1 to 10 % of the clay fraction) or in Mg-claystones with spherulites (present in less than 5 % of the samples and representing 1 to 10 % of the clay fraction). It is absent in the other facies (Fig. 6B).

Non-magnesian clay minerals are mainly illite-smectite and illite. These clays occur in small quantities in about 50 % of all the samples, except for the laminites where illite-smectite is only present in 15 % of the samples but representing more than 50 % of the clay fraction (Fig. 6A). Other minor occurrences of non-magnesian clays in the basin include kaolinite and chlorite.

In terms of stratigraphic distribution, Mg-smectite predominates in Unit 3 and in the lower areas (Fig. 6A). Kerolite and mixed layer kerolite/Mg-smectite contents increase in Units 2 and 1. The highest proportions of kerolite occur in Unit 1, whereas the highest content of mixed-layer kerolite/Mg-smectite occurs in Unit 2, mostly in wells situated in lower areas of the transects. Sepiolite occurs in small quantities in Unit 2, in well W4 (higher domain) (Fig. 6A).

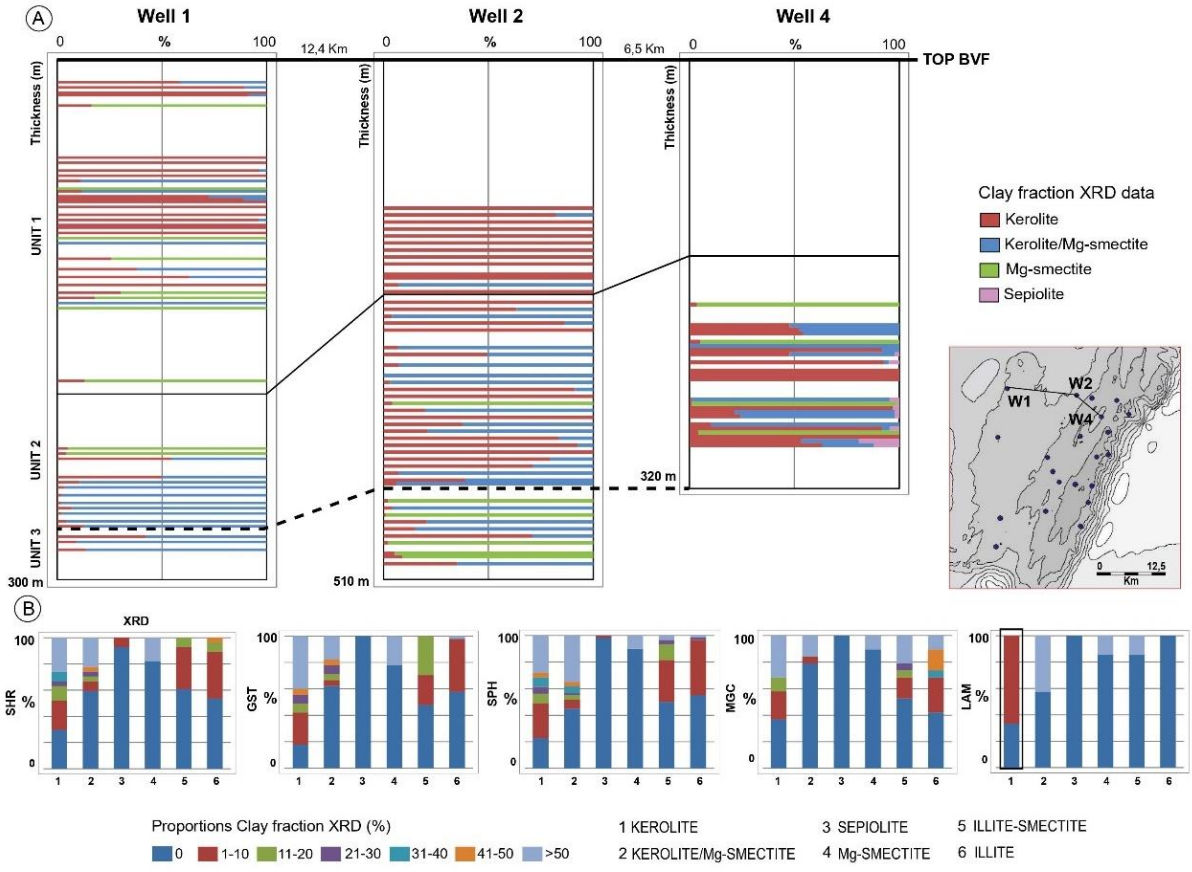


Figure 6 – (A) NW-SE transect showing the spatial and stratigraphic distribution of clay minerals (XRD). The dashed line represents the Intra-Alagoas unconformity. (B) Clay mineral composition per facies (SHR= fascicular calcite crusts, GST= intraclastic grainstones, SPH= Mg-claystones with high spherulite content, MGC= Mg-claystones with low spherulite content, LAM= laminites). The black rectangle on the last diagram is a reading example: for the samples identified as laminites facies, 33 % do not present kerolite, and 67 % present between 1-10 % of kerolite.

## 4.4 Other diagenetic constituents

In the studied carbonate succession, a complex interplay of sedimentary and diagenetic processes occurred, and it is somehow difficult to put a strict boundary between near-surface and burial diagenesis. We followed the diagenetic sequences proposed by Herlinger et al. (2017) and Lima and De Ros (2019), which considered fascicular calcite crusts as essentially syngenetic and spherulites as eogenetic products. Other post-depositional phases are also associated with early diagenesis or even late diagenesis.

480 **4.4.1 Dolomite**

481 Dolomite is one of the most common diagenetic constituents observed in thin sections, occurring with
482 five main fabrics. The first type, only observed locally, forms lamellar aggregates (Fig. 7A), 30 to 50 µm
483 in thickness and composed of fibrous dolomite and magnesite. Some dolomite rhombs grew on the
484 lamellar dolomite. The second type is microcrystalline dolomite, which consists of very fine subhedral
485 crystals (15 to 60 µm) replacing spherulites and Mg-clays (Fig. 7B), as well as the laminites facies, giving
486 a recrystallized mottled aspect. The third type, called rhombohedral dolomite, occurs as well-
487 developed euhedral rhombs (25 to 100 µm in diameter) that can display concentric zonation, and that
488 are commonly arranged in a scattered floating pattern in Mg-clays, with evidence of displacive growth
489 (Fig. 7C). In a few samples, it occurs in the growth-framework porosity of fascicular crusts, showing a
490 tighter idiotopic texture, with no or very rare remnants of clays and a secondary intercrystalline
491 porosity (Fig. 7D). The fourth type is granular mosaic dolomite, that consists of anhedral to subhedral,
492 fine to coarse crystals (0,25 to 1 mm) generally affecting pervasively the original facies, replacing
493 original calcite grains (spherulites, intraclasts…) and growing as a pore-filling cement in the primary
494 porosity (Fig. 7E-7G). This dolomite type also co-occurs with macrocrystalline quartz as fracture-infill
495 (Fig. 7H). Finally, the fifth type is coarse-crystalline saddle dolomite formed of anhedral to subhedral
496 prismatic crystals with sweeping extinction and curved crystal faces (Fig. 7I).
497 Laminites and Mg-claystones with spherulites show the highest contents of dolomite (Table 1).
498 Dolomite is one of the major constituents in the laminites, being present in 93 % of the samples
499 (Supplementary material Fig. A2). Pore-filling, microcrystalline dolomite occurs in 22 % of the samples,
500 but only in small amounts. In the Mg-claystones with higher proportions of spherulites, the dolomite
501 occurs in 94 % of the samples showing an average amount of 25 %. In these samples, the main dolomite
502 fabric is rhombohedral, followed in relative order of importance by microcrystalline and lamellar
503 aggregates. As a pore-filling cement phase, dolomite is present in 22 % of the samples. Mg-claystones
504 with minor proportions of spherulites shows Mg-clay replacement by dolomite in 90 % of the samples,

505 representing average proportions around 27 % per sample, mainly of microcrystalline and
506 rhombohedral types.
507 In fascicular calcite crusts, dolomites occur mainly with its rhombohedral form (Fig. 7D) and as
508 microcrystalline mosaics, with minor occurrences of saddle dolomite. The amount of dolomite per
509 sample can reach 63 % (Table 1), with average values that vary around 13 % per sample. The main form
510 of dolomite occurrence is as replacement of interstitial Mg-clay and shrubs, being present in 66 % of
511 the samples, with average values of 9 % per sample.
512 Pore-filling dolomite cement predominates in the intraclastic grainstones and fascicular calcite crusts,
513 representing a key process of porosity reduction. Dolomite cement occurs in 73 % of the intraclastic
514 grainstone samples, with average quantities of 7 % per sample, and up to 54 % per sample (Table 1).
515 It is represented by rhombohedral and granular mosaic types, and locally by saddle dolomite. 44 % of
516 the fascicular calcite crusts display dolomite cement which may reach up to 63 % per sample.

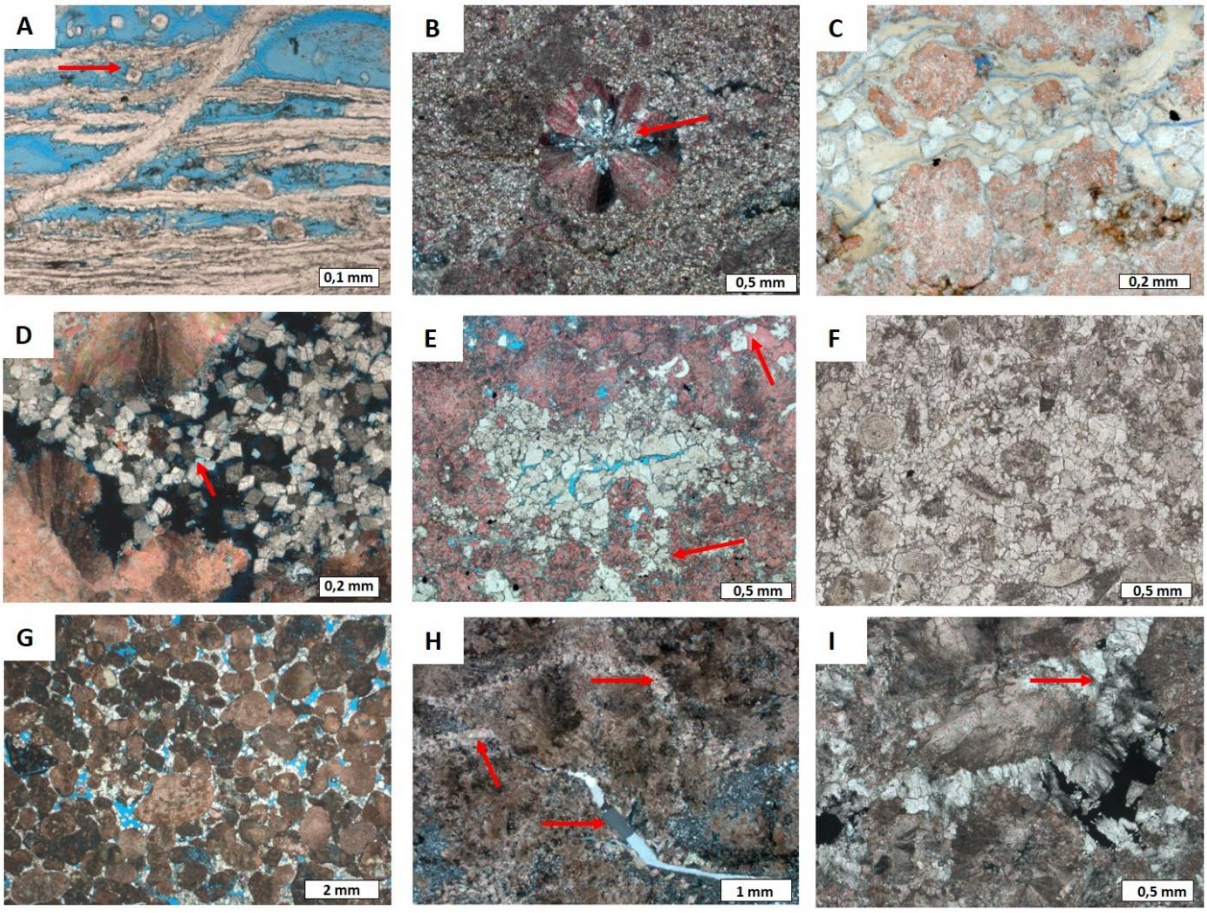

517

Figure 7 – Photomicrographs highlighting different dolomite types of Barra Velha Formation: (A) Lamellar aggregates. The red arrow highlights dolomite rhombs (plane-polarized light; PPL); (B) Very fine dolomite crystals replacing calcite spherulites and possibly matrix (crossed-polarized light; XPL). Note the spherulite partially replaced by quartz (red arrow); (C) Rhombohedral dolomite replacing Mg-clay (PPL); (D) Fascicular calcite crusts with rhombohedral dolomite cement (XPL); (E) In-situ facies with anhedral dolomite cement. The red arrows highlight the carbonate constituents replaced by dolomite (PPL); (F) Grainstone with medium to coarse granular mosaic dolomite (indistinct cement and replacement phase) (PPL); (G) Grainstone with fine granular dolomite cement (PPL); (H) Fascicular calcite crusts intensely replaced by dolomite and quartz. The red arrows highlight the filling of the pore-fracture by dolomite and quartz (XPL); (I) In-situ facies with saddle dolomite. Note the sweeping extinction (red arrow; XPL).

### 4.4.2 Calcite

Even considered eodiagenetic in origin (Herlinger et al., 2017; Lima and De Ros, 2019), the spherulites have been described in sections 4.1.2 and 4.2, as a main component of the Mg-claystones with spherulites facies. Besides the fascicular and spherulitic aggregates, diagenetic calcite occurs also in four various fabrics: 1) crypto- to fine crystalline form; 2) as rim cement; 3) as a coarse-crystalline, granular mosaic; and 4) as a blocky cement mostly filling fractures.

Cryptocrystalline to fine crystalline calcite (Fig. 8A), is formed of inclusion-rich, subhedral crystals (10 to 20 µm) or crystal clusters, that mimic the original facies texture or allochems (lamination, spherulites…), suggesting a replacement process. In some samples, this crystalline fabric is dominant, leading to partial or total recrystallization of the original host. Rarely, calcite rims, 10 to 30 µm thick, formed of prismatic to bladed crystals are observed as a coating around grains, in grainstones facies (Fig. 8B). Rims are associated mainly with Mg-clay ooids (Fig. 8C). The coarse-crystalline calcite is composed of medium to coarse (100 to 500 µm), anhedral to subhedral crystals, filling the porosity in a granular, equant mosaic fabric (Fig. 8C). This calcite grows in facies that have previously undergone compaction, attested by the concave-convex sutures between grains (Fig. 8D). Finally, minor amounts of coarse euhedral crystals, poikilotopic and blocky calcites are also recognized, as a cement phase, essentially filling fractures (Fig. 8E). This blocky calcite engulfs the saddle dolomite cement, thus postdating it (Fig. 8F).

548 Diagenetic calcite occurs mainly in laminites, Mg-claystones, and grainstones facies (Table 1,
549 supplementary material Fig. A3). Cryptocrystalline to fine-crystalline calcite is present in about 40 % of
550 the laminites and claystones samples, with more than 30 % as a replacement phase. Calcite pore-filling
551 cement is common in grainstones (Fig. 8B and 8C), with 20 % of the samples presenting more than 10
552 % of calcite cement. Mosaic calcite occurs in 42 % of the samples, and calcite rims in 10 % of the
553 samples. In the fascicular calcite crusts, different types of diagenetic calcite are present in 47 % of the
554 samples, occurring similarly as a cement and a replacement phase. The most common fabrics observed
555 in the fascicular calcite crusts are, in order of relative importance, medium to coarse-crystalline mosaic
556 (cement phase), fine-crystalline calcite (replacement) and coarse euhedral blocky calcites (cement).
557 Minor occurrences of blocky calcite filling fractures and rims can be seen in up to 10% of the samples.
558

559 **4.4.3 Silica**

560 Silica is common in the BVF and displays four main different fabrics. Crypto- to microcrystalline silica
561 is the most frequent silica phase, forming drusy aggregates that partially to totally silicified calcite
562 spherulites (Fig. 7B), and mimetically replaced Mg-clay matrix. The silica replacement can be fabric
563 selective (e.g., it is confined within selected grains) or non-selective (Fig. 8G). This phase can also fill
564 growth-framework porosity between fascicular calcite crusts (Fig. 8H). Reworked silicified spherulites
565 and intraclasts in the grainstone facies tend to indicate an early process of silicification.
566 Microcrystalline silica is generally associated with microporosity. Quartz rims (20 to 50 µm thick) are
567 observed locally, forming coatings around grains made of prismatic to bladed crystals (Fig. 8C and 8I).
568 These rims predate the development of coarse-crystalline mosaic calcite (Fig. 8C). The similar
569 crystalline fabric, scale, occurrence in grainstone facies suggest a possible replacement of calcite rims
570 by silica. The third type is macrocrystalline quartz, composed of subhedral to anhedral crystals, 30 to
571 100 µm in diameter, that form a coarse mosaic cement filling pores (Fig. 8I) and also observed as
572 fracture infills. It is unclear if this phase may also be replacive. Last, a chalcedony phase with a fibrous

radiated fabric is observed and partially engulfs and replaces the coarse-crystalline mosaic and the blocky calcites (Fig. 8E and 9A).

The laminites contains the largest amount of silica, primarily as a replacement phase, being present in 70% of the samples (Supplementary material Fig. A4). Centimetric tabular laminae and nodules of silica, evolved in a few cases to pervasive silicification. Microcrystalline quartz is the most common silica form in laminites, followed by chalcedony and macrocrystalline mosaic quartz.

The replacement of Mg-clays and calcite spherulites by silica is also frequently observed and occurs mainly as microcrystalline and macrocrystalline mosaic quartz. In the Mg-claystones with higher spherulite contents, silicification is observed in 75 % of the samples. In the fascicular calcite crusts, the replacement reaches a maximum of 65 % of the samples, but in general, the proportion per sample is low, with an average of 4 %. Chalcedony is accessory and mainly replaces spherulites and fascicular calcite.

As for calcite, pore-filling silica is more important in the fascicular calcite crusts and intraclastic grainstones (Fig. 8G and 8H). The proportions are similar in both facies (Table 1) and quartz as a pore-filling phase is present in 40 % of the fascicular calcite crusts samples and in 35 % of the grainstone samples.

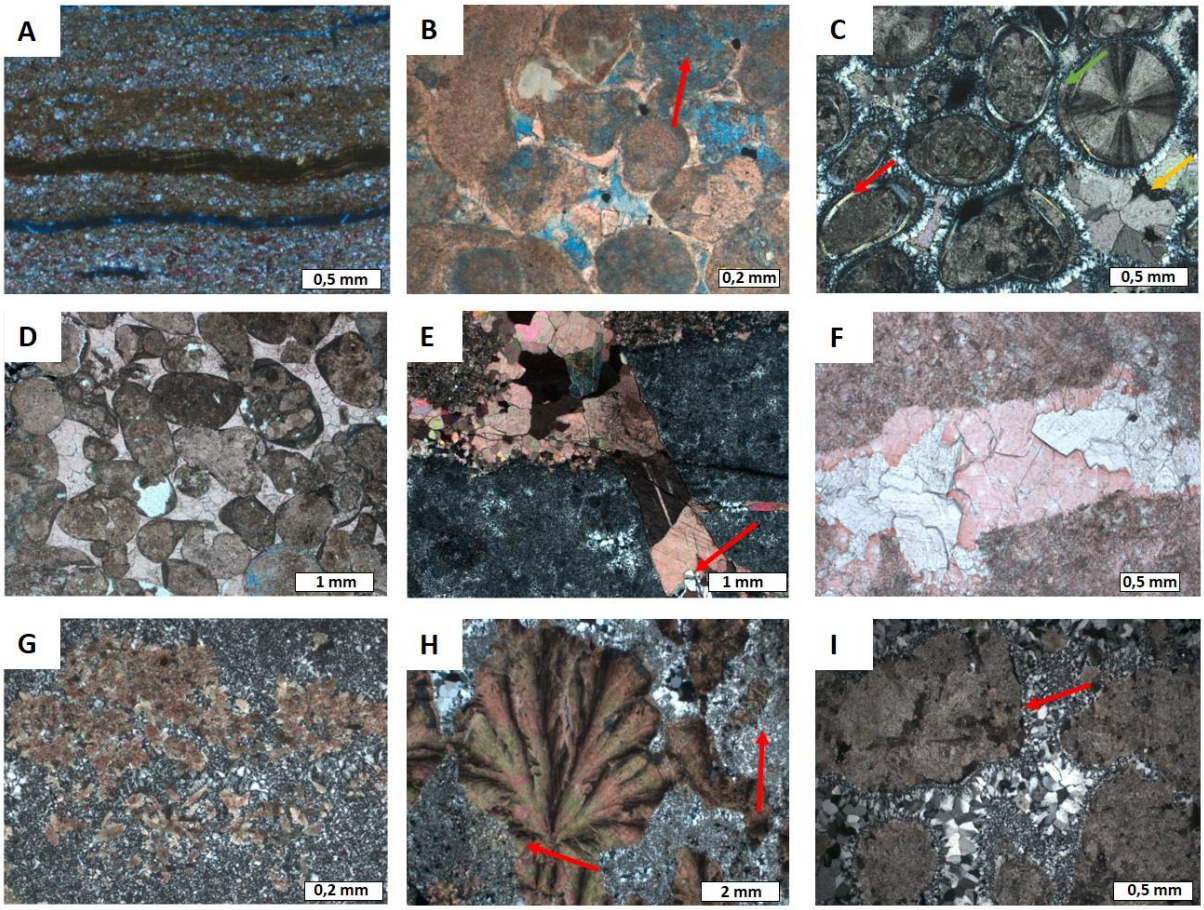


Figure 8 - (A) Mg-clay partially replaced by very fine calcite and dolomite crystals (crossed-polarized light, XPL); (B) Grainstone constituents with calcite rims. Note the dissolution of the carbonate intraclasts (plane-polarized light, PPL); (C) Grainstone with fragments of shrubs, spherulites, showing silica rims and Mg-clay envelops (red arrow). The yellow arrow highlights mosaic calcite filling porosity, the green arrow highlights calcite coating around grains (XPL); (D) Grainstone with blocky calcite cement (PPL); (E) Poikilotopic calcite, filling fracture (XPL), partially replaced by chalcedony (red arrow); (F) In-situ facies with blocky calcite engulfing saddle dolomite cement (PPL); (G) In-situ facies with intense silicification (XPL); (H) Fascicular calcite crust with quartz cement. Note the quartz replacing the fascicular calcite (red arrows); (I) Grainstone with silica rims (red arrow) and macrocrystalline quartz cement (XPL).

### 4.4.4 Minor diagenetic phases

Minor occurrences of replacive and pore-filling minerals including barite, celestite, cryolite, dawsonite, fluorite, illite/smectite, kaolinite, and magnesite have been observed (Table 1). Magnesite, dawsonite and barite are the most frequent. Magnesite is present in 25 % of the Mg-claystones with spherulites and occurs as lamellar aggregates replacing and filling shrinkage pores in the Mg-clays. Dawsonite

608 occurs mostly associated with fascicular calcite crusts and spherulites (Fig. 9B) and barite occurs mainly
609 as a cement phase in intraclastic grainstones and fascicular calcite crusts (Fig. 9C).
610
611 **4.4.5 Dissolution and fractures**
612 Secondary porosity is generated by the dissolution of both Mg-clays and carbonate constituents.
613 Dissolution of carbonate intraclasts generated intraparticle and moldic porosity on intraclastic
614 grainstones (Fig. 8B). In fascicular calcite crusts, dissolution generated intra-framework porosity. In
615 these facies, the enlargement of interparticle and growth-framework pores is also common, creating
616 larger vugs (Fig. 9D). In laminites facies, a matrix microporosity is observed (Fig. 9E) as well as a
617 fenestral porosity, locally enlarged due to dissolution. In Mg-claystones, porosity formation is specially
618 related to Mg-clay dissolution (Fig. 9F), although the dissolution of spherulites is significant in some
619 samples. Dissolution of pore-filling calcite cement phase is common, generating intracrystalline
620 porosity. Porosity generated by dissolution is observed in different proportions in all the facies,
621 although preferentially affecting fascicular calcite crusts, Mg-claystones with spherulites, and
622 intraclastic grainstones (Table 1).
623 Late cement phases filling secondary dissolution pores are often observed, mainly in fascicular calcite
624 crusts and Mg-claystones with spherulites. In fascicular calcite crusts, late cements can consist of 35 %
625 of dolomite, and 25 % of calcite. Fractures are observed mainly in intraclastic grainstones and fascicular
626 calcite crusts and are frequently filled by a cement of quartz and calcite. However, the occurrence in
627 the samples is local.

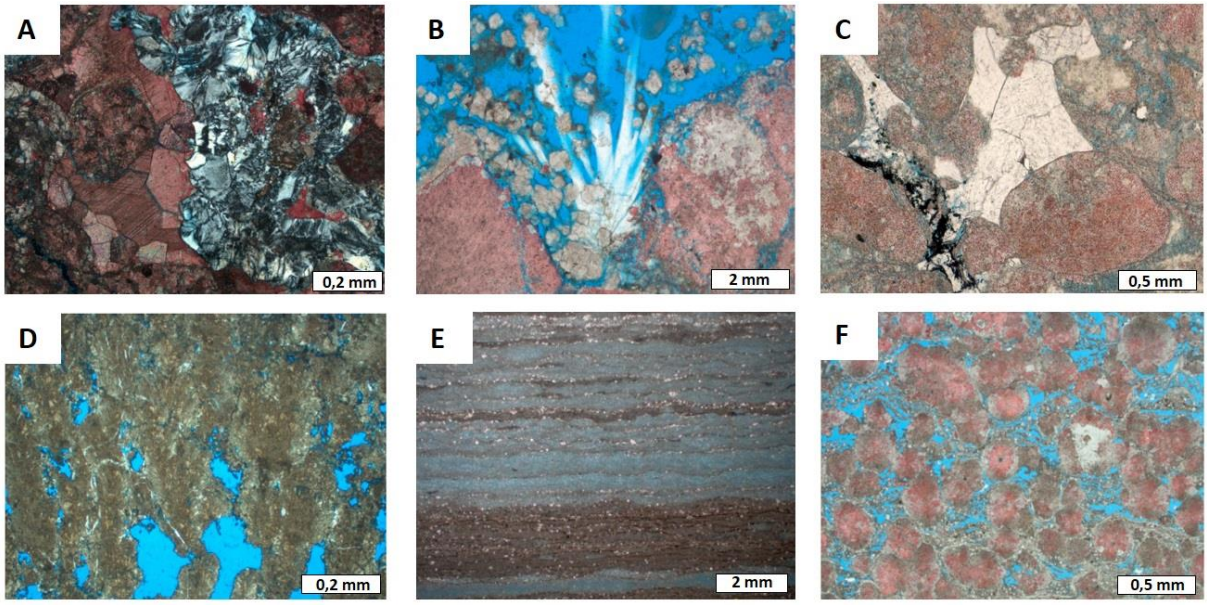


628

629 Figure 9 – (A) Grainstone with coarse mosaic calcite, replaced by chalcedony (crossed polarized light;
630 XPL); (B) Fascicular calcite crusts with cement of dawsonite and euhedral dolomite (plane-polarized
631 light, PPL); (C) Cement of dawsonite and euhedral dolomite (PPL); (D) Growth-framework porosity
632 enlarged by dissolution (PPL); (E) General aspects of dissolution in laminites; (F) General aspects of
633 dissolution on Mg-claystones with spherulites (PPL).

634

635 **4.5 Distribution of the diagenetic phases and dissolution**

636 The results of petrographic observations and quantification were set in the studied wells, organized
637 along two dip transects, perpendicular to the structural high (Figs. 10 and 11) and one strike transect
638 along the SE flank, parallel to the structural high (Fig. 12). Vertical sampling spacing varies from 30 cm
639 to 5 m, with an average spacing of 50 cm. The dataset enables the characterization of the lateral and
640 vertical distribution of the main diagenetic phases (Fig. 13).

641 The northeastern region of the study area (transect A, Fig. 10) shows a higher proportion of dolomite
642 in the transitional zone and towards the structural high. This increase is associated with the
643 replacement of the constituents, and partially with a pore-filling cement phase (Fig. 10A and B).
644 Conversely, in the central portion of the study area, represented by transect B, dolomitization
645 increases towards the lower area, especially in Unit 1 (Fig. 11B). Dolomitization is also intense in the
646 wells of the southeast flank, both in Units 2 and 1 (Fig. 12B). In this area, dolomite cement is frequent

(Fig. 12A), mostly in intraclastic grainstones. The increase of dolomite in lower sites, as observed in transect B (Fig. 11), may be related to differences in the structural pattern of the study area. The region of well W6 is marked by a higher relief bounded by faults (Fig. 1C and Fig. 11), creating a distinct depositional setting compared with the northwest portion.

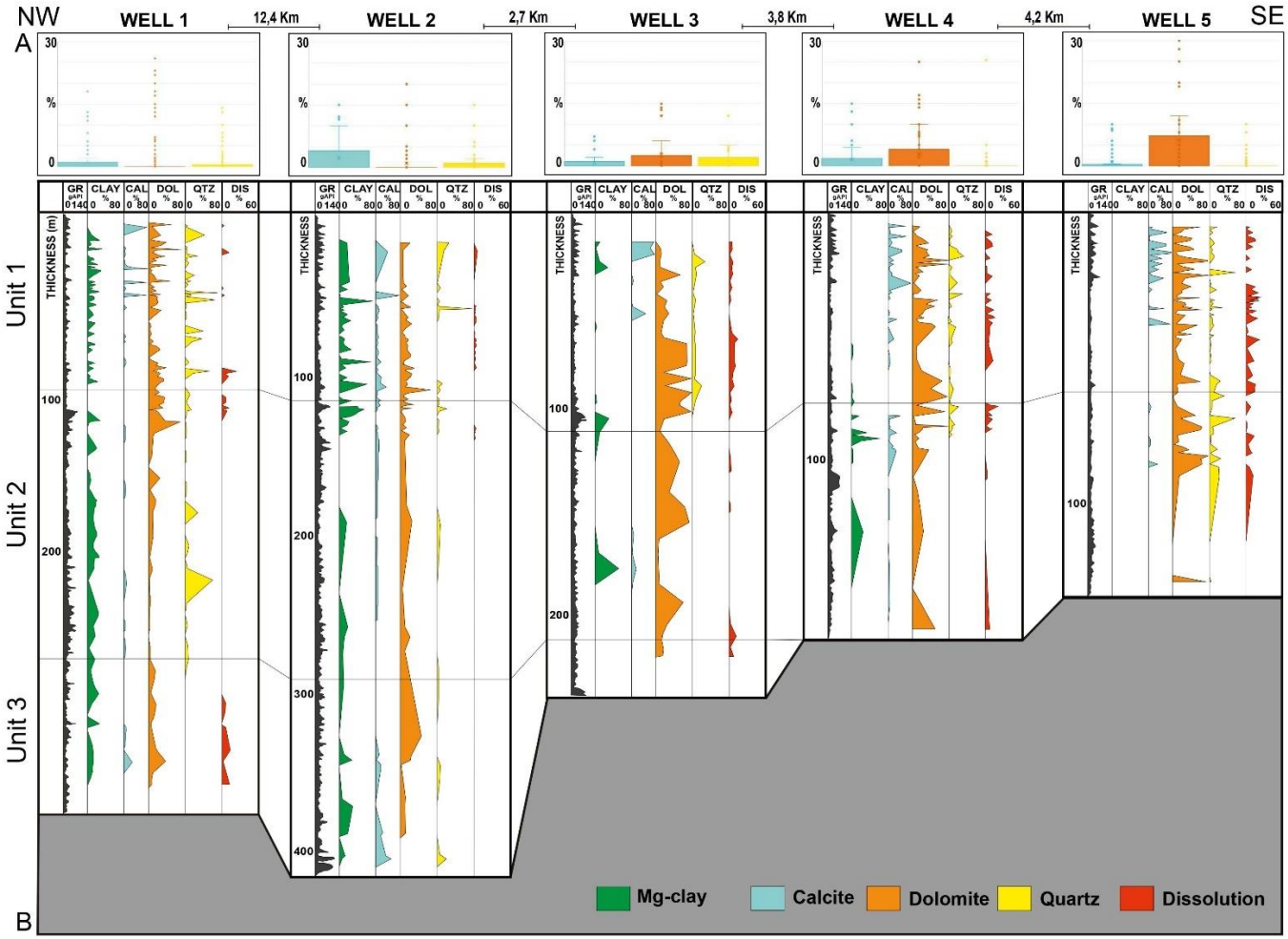


Figure 10 – NW-SE correlation along transect A showing the quantitative distribution of the main diagenetic minerals in the study area. A) Boxplots of calcite, dolomite, and quartz pore-filling cement proportions. B) Vertical distribution of Mg-clay, diagenetic minerals (sum of the replacement and cementation) and dissolution. Values vary between 0 and 80% per sample for the Mg-clay and diagenetic minerals and between 0 and 60% for the dissolution process. The gamma ray log (GR) is also plotted. The profile morphology was reconstructed based on the BVF basal boundary assessed from seismic interpretation (Artagão, 2018), corroborated with the well data that reach the BVF boundary.

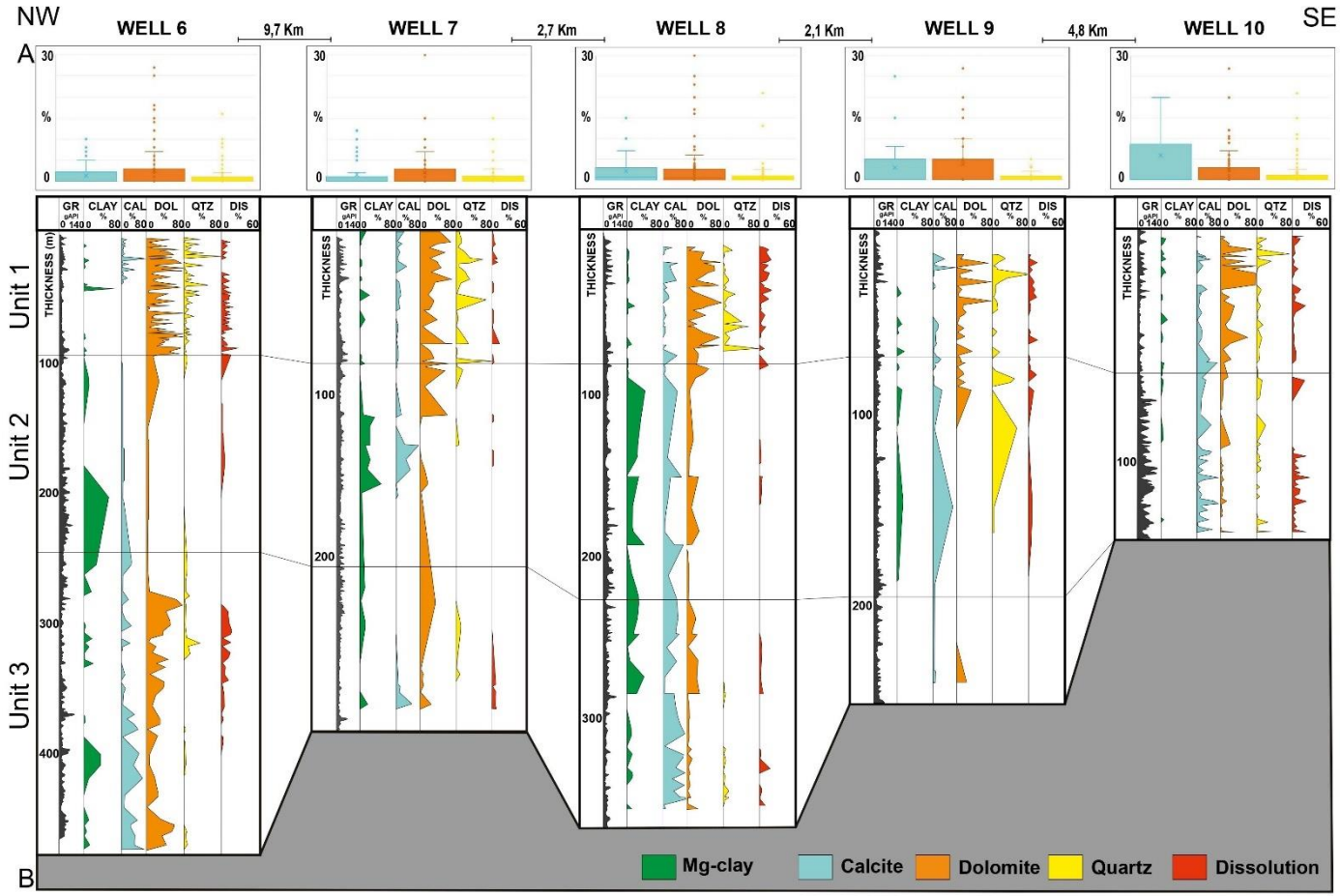


Figure 11 – NW-SE correlation along transect B showing the quantitative distribution of the main diagenetic minerals in the study area. A) Boxplots of calcite, dolomite, and quartz pore-filling cement proportions. B) Vertical distribution of Mg-clay, diagenetic minerals (sum of the replacement and cementation) and dissolution. Values vary between 0 and 80% per sample for the Mg-clay and diagenetic minerals and between 0 and 60% for the dissolution process. The gamma ray log (GR) is also plotted. The profile morphology was reconstructed based on the BVF basal boundary assessed from seismic interpretation (Artagão, 2018), corroborated with the well data that reach the BVF basal boundary.

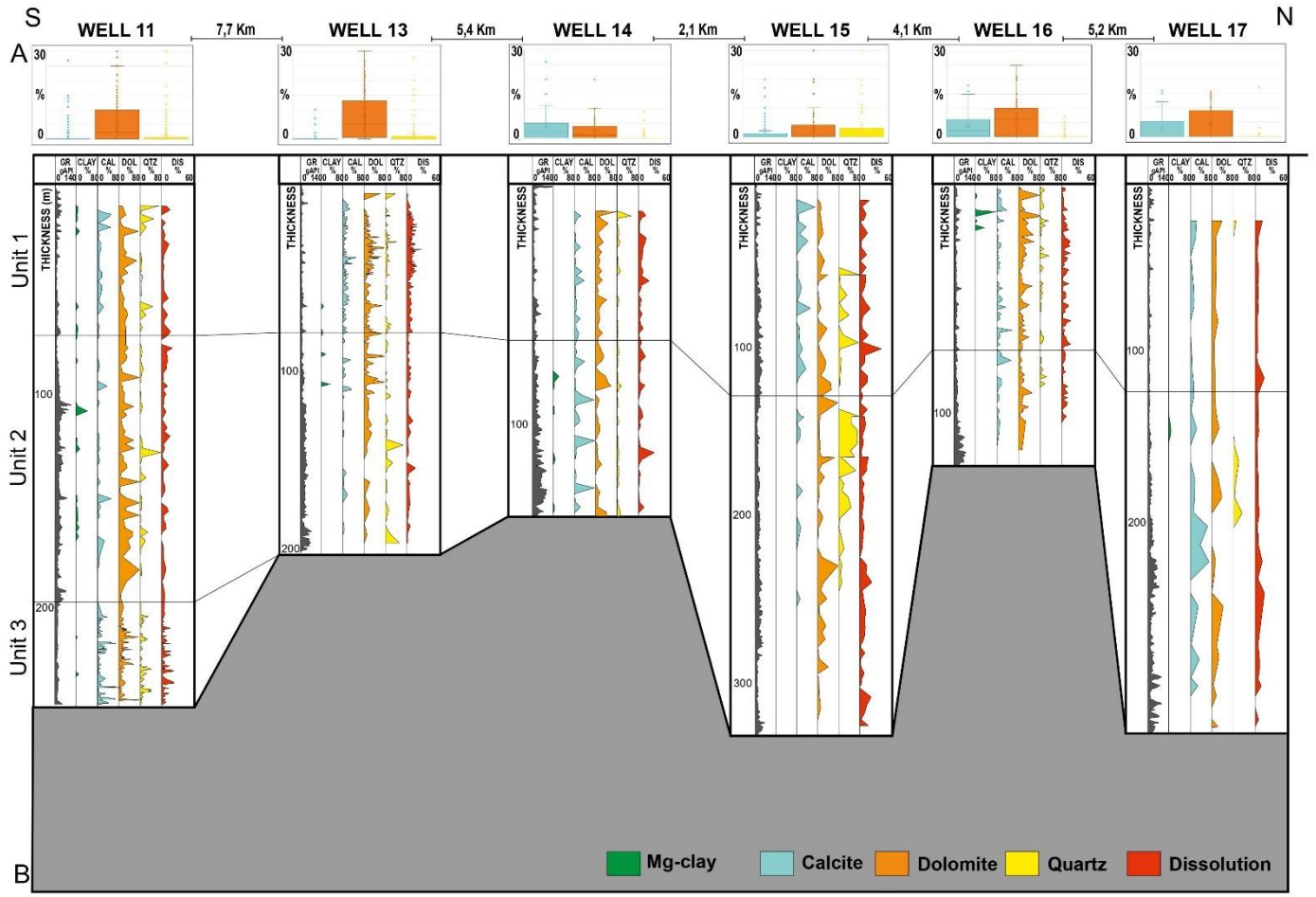


Figure 12 – NW-SE correlation along transect C showing the quantitative distribution of the main diagenetic minerals in the study area. A) Boxplots of calcite, dolomite, and quartz pore-filling cement proportions. B) Vertical distribution of Mg-clay, diagenetic minerals (sum of the replacement and cementation) and dissolution. Values vary between 0 and 80% per sample for the Mg-clay and diagenetic minerals and between 0 and 60% for the dissolution process. The gamma ray log (GR) is also plotted. The profile morphology was reconstructed based on the BVF boundary assessed from seismic interpretation (Artagão, 2018), corroborated with the well data that reach the BVF boundary.

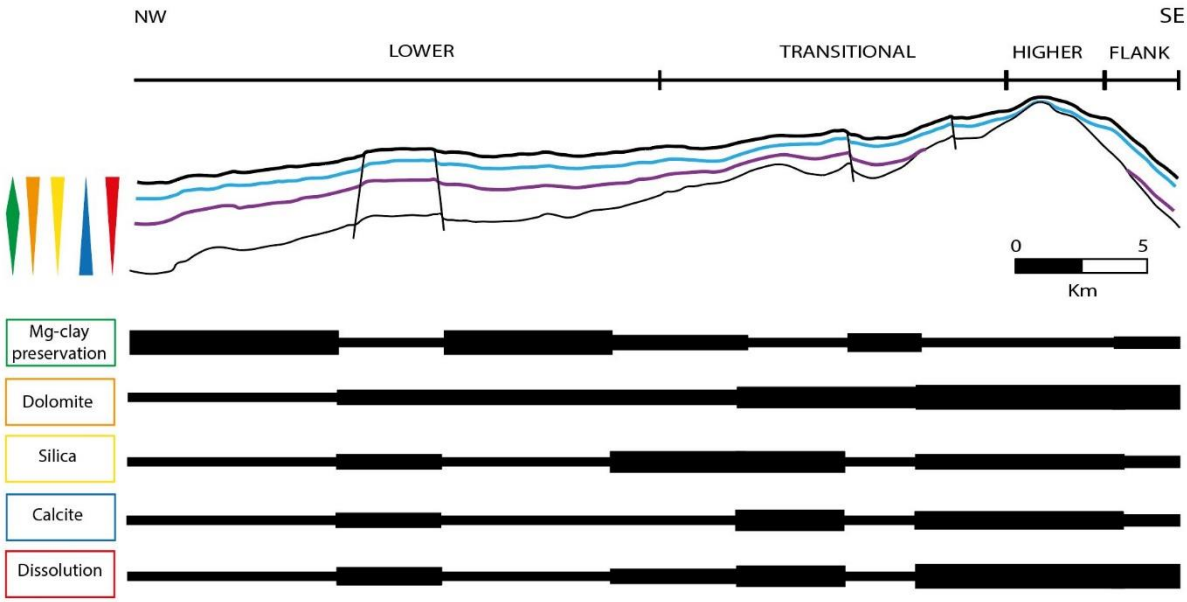


Figure 13 – Scheme showing the lateral and vertical distribution of the main diagenetic phases in the study area. Purple line represents the Intra-Alagoas unconformity (between Unit 3 and 2) and the blue line represents the boundary between Units 2 and 1.

Dolomite fabrics also spatially vary. The highest amounts and proportion per sample of rhombohedral dolomite are observed in lower areas (Fig. 14). Rhombohedral dolomite is widely found associated with Mg-claystones with spherulites and fascicular calcite crusts facies. Medium-crystalline mosaic dolomite has similar proportions in all the facies and is most common on the structural highs. An important increase of mosaic dolomite is observed in Unit 1. Microcrystalline dolomite is also abundant, prevailing in the laminites, and transitional areas (Fig. 14). The other dolomite types occur locally but can reach 90 % in some samples, as in the case of saddle dolomite. The proportion of lamellar dolomite/magnesite is in general, very low, but it is possible to observe a preferential association of lamellar aggregates with fascicular calcite crusts and spherulitic facies.

Calcite cementation generally occurs in the highest structural parts, and on the southeastern flank (Figs. 11A and 12A). It is also more abundant in Units 2 and 3, in the central region (transect B; Fig. 11), associated with reworked facies (intraclastic grainstones). Other major occurrences are observed in Unit 1, associated with crenulated laminites. The coarse-crystalline mosaic and blocky calcites are

more developed in the southeast flank. Although the calcite rims occur in small proportion, they are also more frequent in the southeast flank and on the structural high.

Silica does not present any peculiar spatial distribution, although it is possible to observe higher proportions in Unit 1 (Fig. 12), preferentially in the laminites facies, and along the southeastern flank, essentially as a cement phase (Fig. 11B). Chalcedony is found mainly in Mg-claystones with spherulites and in fascicular calcite crusts on the southeastern flank and the structural high, and occasionally in the lower areas (Table 3). Among other diagenetic phases, dawsonite and barite are the most frequent, both occurring as replacement and cement. Dawsonite follows the same distribution pattern as chalcedony, while barite occurs primarily as a cement phase on the southeastern flank, mainly in Unit 1.

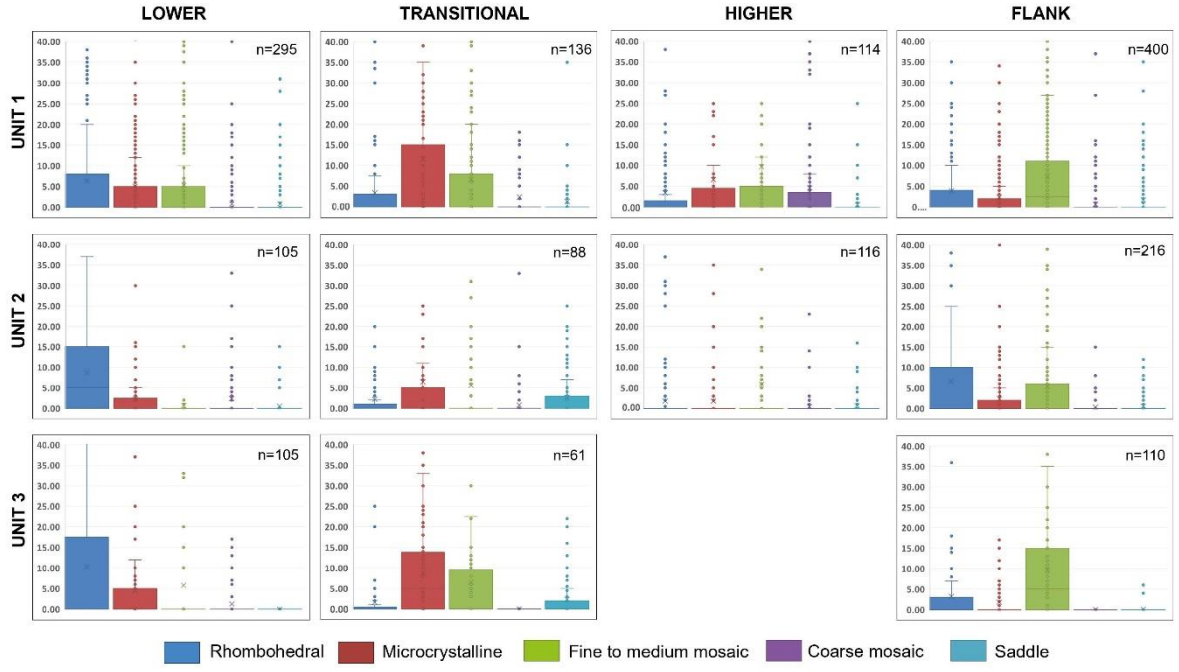


Figure 14 – Boxplots showing the distribution of the different types of dolomite, in different parts of the study area and stratigraphic units. No data was collected for Unit 3 in the higher area, as it pinches out. The data of Unit 3 in the flank region are from well W11.

Dissolution increases towards the structural high (Fig. 10 and 11) and is widely observed in the southeastern flank (Fig. 12). In the lower areas, dissolution is important only in Unit 1. In this stratigraphic unit, Mg-claystones with spherulites show major dissolution features, as well as the

laminites. The largest occurrences of vuggy pores are also concentrated in Unit 1, mainly associated with fascicular calcite crusts in the higher area of the depositional profile. In the southeastern flank, dissolution frequently occurs in both Units 1 and 2. A punctual increase in Unit 3 of well W6 is also observed (Fig. 11). Post-dissolution cementation is localized and occurs mainly in the transitional and higher areas.

Average porosity values generated by dissolution are low (Tables 2 and 3), but this represents only the dissolution porosity quantified by petrography. At a larger scale, core description shows that dissolution is intense and pervasive in the wells situated in the structural highs, where it can be associated with fracturing. The statistical analysis of the petrographic data indicates this general trend of dissolution.

Table 2 – Statistical summary of the average and maximum amounts of major diagenetic constituents, Mg-clay, and secondary porosity, in the stratigraphic units of Barra Velha Formation.

| **Stratigraphic unit** | | **Unit 1** | | **Unit 2** | | **Unit 3** | |
|---|---|---|---|---|---|---|---|
| **Constituents (%)** | | Average | Maximum | Average | Maximum | Average | Maximum |
| **Calcite** | Fascicular crusts | 17.90 | 90.00 | 16.10 | 87.00 | 22.30 | 84.00 |
| | Spherulites | 17.60 | 86.00 | 20.20 | 85.00 | 14.90 | 76.00 |
| | **Other diagenetic phases** | | | | | | |
| **Mg-clay** | Syngenetic | 9.00 | 83.00 | 10.00 | 93.00 | 7.00 | 77.00 |
| **Calcite** | Replacing constituents | 4.50 | 90.50 | 3.85 | 75.00 | 10.20 | 85.00 |
| | Filling primary porosity | 2.52 | 34.00 | 2.82 | 78.00 | 4.17 | 52.00 |
| | Filling secondary dissolution porosity | 0.25 | 10.00 | 0.27 | 25.00 | 0.33 | 25.50 |
| | Filling fracture porosity | 0.09 | 8.00 | 0.02 | 5.00 | 0.07 | 5.00 |
| **Dolomite** | Replacing constituents | 16.70 | 86.50 | 10.70 | 90.00 | 11.40 | 93.00 |
| | Filling primary porosity | 4.65 | 52.00 | 4.00 | 63.00 | 4.30 | 55.00 |
| | Filling secondary dissolution porosity | 0.68 | 35.00 | 0.37 | 35.00 | 0.24 | 15.00 |
| | Filling fracture porosity | 0.01 | 5.00 | 0.001 | 1.00 | - | - |
| **Silica** | Replacing constituents | 5.80 | 97.00 | 2.90 | 78.00 | 1.60 | 25.00 |
| | Filling primary porosity | 1.70 | 33.00 | 1.03 | 58.00 | 1.60 | 52.00 |
| | Filling secondary dissolution porosity | 0.30 | 16.00 | 0.24 | 15.00 | 0.50 | 18.00 |
| | Filling fracture porosity | 0.04 | 8.00 | 0.004 | 1.00 | 0.10 | 10.00 |
| **Secondary dissolution porosity** | | 5.00 | 40.00 | 4.00 | 30.00 | 3.00 | 22.00 |
| **Detrital grains** | | 3.00 | 30.00 | 4.00 | 18.00 | 6.00 | 34.00 |

720 Table 3- Statistical summary of the average and maximum amounts of major diagenetic constituents,
721 Mg-clay, and secondary porosity of Barra Velha Formation, in different portions of the study area.

| Regions | | Lower | | Transitional | | Higher | | Flank (section C) | |
|---|---|---|---|---|---|---|---|---|---|
| Constituents (%) | | Average | Maximum | Average | Maximum | Average | Maximum | Average | Maximum |
| Calcite | Fascicular crusts | 12.5 | 83.0 | 13.4 | 87.0 | 17.5 | 90.0 | 20.0 | 84.0 |
| | Spherulites | 26.7 | 86.0 | 14.5 | 72.0 | 14.0 | 66.0 | 12.8 | 62.0 |
| | **Other diagenetic phases** | | | | | | | | |
| Mg-clay | Syngenetic | 10.0 | 75.0 | 6.0 | 51.0 | 1.0 | 39.0 | 1.0 | 42.0 |
| Calcite | Replacing constituents | 5.2 | 90.5 | 10.48 | 75.0 | 5.8 | 70.0 | 3.0 | 85.0 |
| | Filling primary porosity | | 30.0 | 1.51 | 52.0 | 3.5 | 67.0 | 4.12 | 78.0 |
| | Filling secondary dissolution porosity | 0.39 | 8.0 | 0.77 | 25.5 | 0.25 | 10.0 | 0.05 | 5.0 |
| | Filling fracture porosity | 0.08 | 5.0 | 0.01 | 1.5 | 0.04 | 3.0 | 0.09 | 8.0 |
| Dolomite | Replacing constituents | 17.5 | 86.0 | 19.0 | 93.0 | 13.6 | 86.5 | 10.2 | 90.0 |
| | Filling primary porosity | 2.08 | 45.0 | 2.6 | 30.0 | 3.4 | 51.0 | 6.5 | 63.0 |
| | Filling secondary dissolution porosity | 0.2 | 10.0 | 0.79 | 30.0 | 0.76 | 35.0 | 0.5 | 35.0 |
| | Filling fracture porosity | 0.006 | 2.0 | 0.004 | 0.5 | 0.02 | 5.0 | 0.001 | 1.0 |
| Silica | Replacing constituents | 3.82 | 97.0 | 4.76 | 78.0 | 3.09 | 70.0 | 4.8 | 72.0 |
| | Filling primary porosity | 0.64 | 27.0 | 1.07 | 53.0 | 0.76 | 15.0 | 2.3 | 58.0 |
| | Filling secondary dissolution porosity | 0.5 | 16.0 | 0.38 | 12.0 | 0.29 | 15.0 | 0.21 | 18.0 |
| | Filling fracture porosity | 0.03 | 3.0 | 0.04 | 3.0 | 0.12 | 8.0 | 0.03 | 10.0 |
| Baryte | Replacing constituents/Filling porosity | 0.03 | 3.5 | 0.06 | 4.0 | 0.12 | 7.0 | 0.07 | 5.0 |
| Chalcedony | Replacing constituents/Filling porosity | 0.5 | 40.0 | 1.0 | 35.0 | 2.4 | 70.0 | 0.9 | 80.0 |
| Dawsonite | Replacing constituents/Filling porosity | 0.03 | 4.0 | 0.07 | 5.0 | 0.05 | 3.0 | 0.3 | 6.0 |
| Secondary dissolution porosity | | 3.0 | 25.0 | 3.0 | 17.0 | 5.0 | 28.0 | 6.0 | 40.0 |
| Detrital grains | | 4.0 | 34.0 | 4.0 | 30.0 | 3.0 | 13.0 | 3.0 | 30.0 |

722

723

724 ## 4.6 Geochemistry

725 ### 4.6.1 Bulk oxygen and carbon isotopic analysis

726 The bulk sample values of $\delta^{13}C$ vary between -1.35 and +4.42 ‰, with median and average values of
727 +2.51 and +2.36 ‰ respectively, and most of the data presenting positive values. The values of $\delta^{18}O$
728 vary between -5.93 and +5.26 ‰, with median and average values of +1.39 and +1.42 ‰, respectively.
729 In contrast to the $\delta^{13}C$ data, the $\delta^{18}O$ displays more negative values, especially in well W6. The bulk
730 sample values of $\delta^{13}C$ and $\delta^{18}O$, categorized by facies and stratigraphic units are shown in Figures 15A
731 and 15B. As bulk analyses are problematic to interpret, data were sorted given their dominant
732 mineralogy, and a selection of samples were realized (Table 4): samples with more than 70 % of the
733 carbonate phase being calcite (mostly fascicular calcite or spherulites) and samples with more than 70

% of the carbonate phase being dolomite (mostly microcrystalline and rhombohedral dolomite). The isotopic data do not show any good covariant trend, whatever the facies, the dominant mineralogy, or the stratigraphic unit (Table 4).

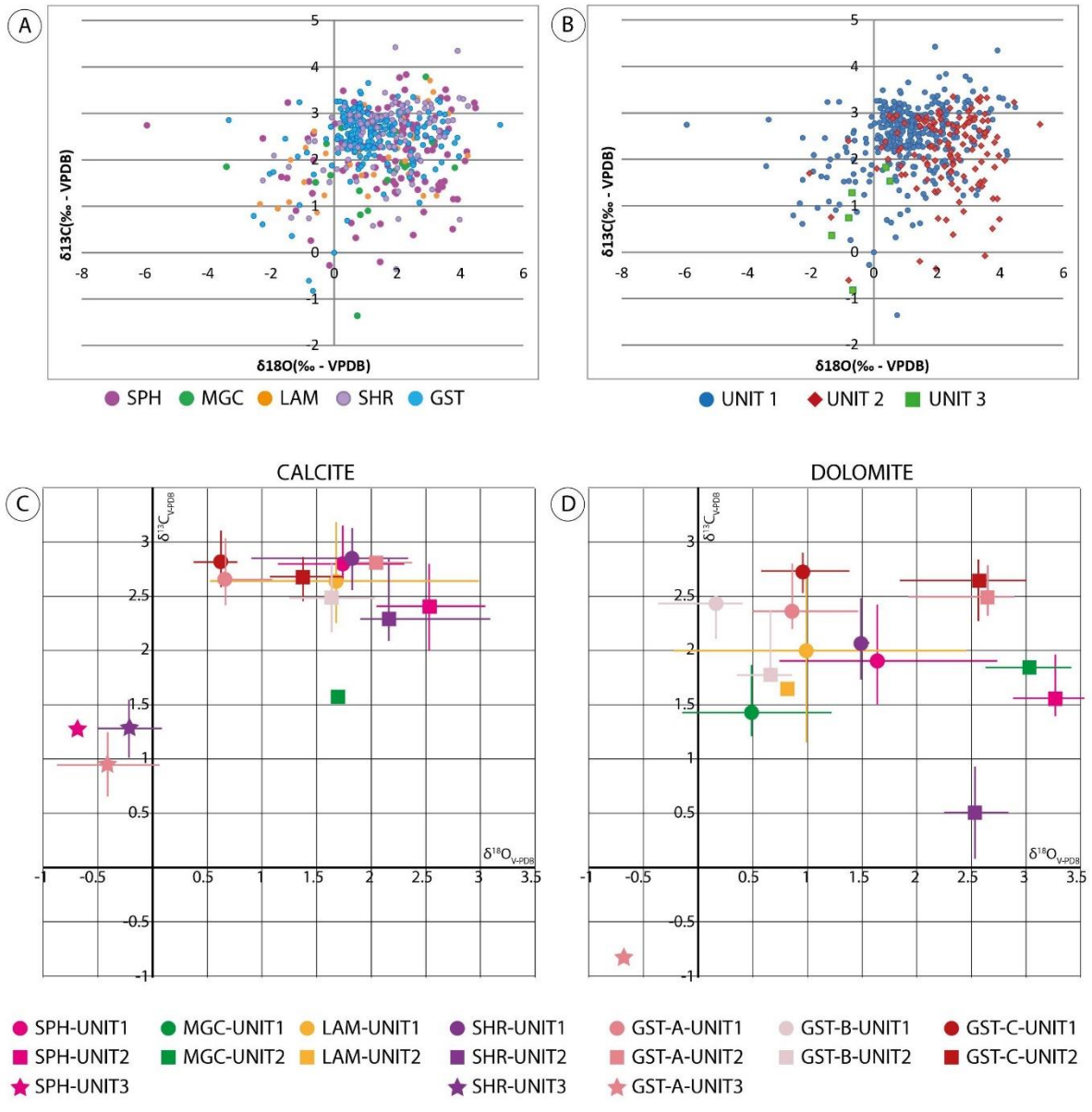


Figure 15 - $\delta^{18}O$ vs. $\delta^{13}C$ crossplots. (A) Bulk values per facies; (B) Bulk values per stratigraphic units; (C) Samples dominated by calcite; (D) Samples dominated by dolomite. For (C) and (D), points correspond to the average values of $\delta^{18}O$ and $\delta^{13}C$ for the different facies and stratigraphic units. The horizontal and vertical bars correspond to the first and third quartile of each dataset (when available). SPH= Mg-claystones with higher spherulite content, MGC= Mg-claystones with lower spherulites content, LAM= laminites, SHR= fascicular calcite crusts, GST= grainstones of different types (A, B, C).

746 Concerning the calcite values, no specific pattern is observed between the stable isotopes and the
747 different facies (Fig. 15C). The data show lower variation ranges for $\delta^{13}C$ than for $\delta^{18}O$ values. A good
748 correlation is observed with stratigraphic units. In Unit 3, at the base of the succession, the low number
749 of samples precludes to make an accurate evaluation of the data, although a few samples show the
750 lowest values with average $\delta^{18}O$ values ranging from -0.69 to -0.21 ‰ and average $\delta^{13}C$ from 0.95 to
751 1.28 ‰. Unit 2 displays the highest $\delta^{18}O$ values (up to 2.53 ‰) and moderate to high average $\delta^{13}C$
752 (from 1.56 to 2.80 ‰). Finally, Unit 1, at the top of the succession is characterized by significantly lower
753 $\delta^{18}O$ values compared to Unit 2 (from 0.62 to 1.82 ‰) but with the highest average $\delta^{13}C$ values (2.63
754 to 2.84 ‰). In this latter unit, it must be noted that a slightly increasing trend of both $\delta^{18}O$ and $\delta^{13}C$
755 average values is observed between the laminites, Mg-claystones with spherulites and shrubs facies.
756 Nevertheless, the $\delta^{13}C$ and $\delta^{18}O$ patterns depend on the location of the wells on the depositional profile
757 (Fig. 16). In well W4, situated on a lower area within the structural high, the $\delta^{13}C$ values are relatively
758 constant, while the $\delta^{18}O$ values present significant differences between the Units 1 and 2. Relative to
759 mineralogy, the highest values of $\delta^{18}O$ are associated with the intervals with high Mg-clay content. In
760 well W5, situated on a higher structural position, a change in $\delta^{13}C$ pattern is observed, with higher
761 values in the Unit 1, whereas $\delta^{18}O$ data show a minor variation. The amount of XRD data in well W5 is
762 insufficient to correlate the isotopic data with mineralogy.
763 The dolomite values show a more scattered distribution (Fig. 15D). As for calcite, no clear relationship
764 is observed between the isotopic signatures and the different facies. The laminites and the type-B
765 grainstones, dominated by microcrystalline dolomites, shows relatively lower $\delta^{13}C$ and $\delta^{18}O$ average
766 values, compared to the other facies, both in Units 1 and 2. The other facies, rather dominated by
767 rhombohedral dolomite show the same stratigraphic trends than for calcite. Thus, Unit 2 shows the
768 highest $\delta^{18}O$ values (up to 3.28 ‰) and highly variable average $\delta^{13}C$ (from 0.50 to 2,64 ‰), while Unit
769 1 is characterized by lower $\delta^{18}O$ values (from 0.17 to 1.64 ‰) but with the highest average $\delta^{13}C$ values
770 (1.42 to 2.72 ‰).
771

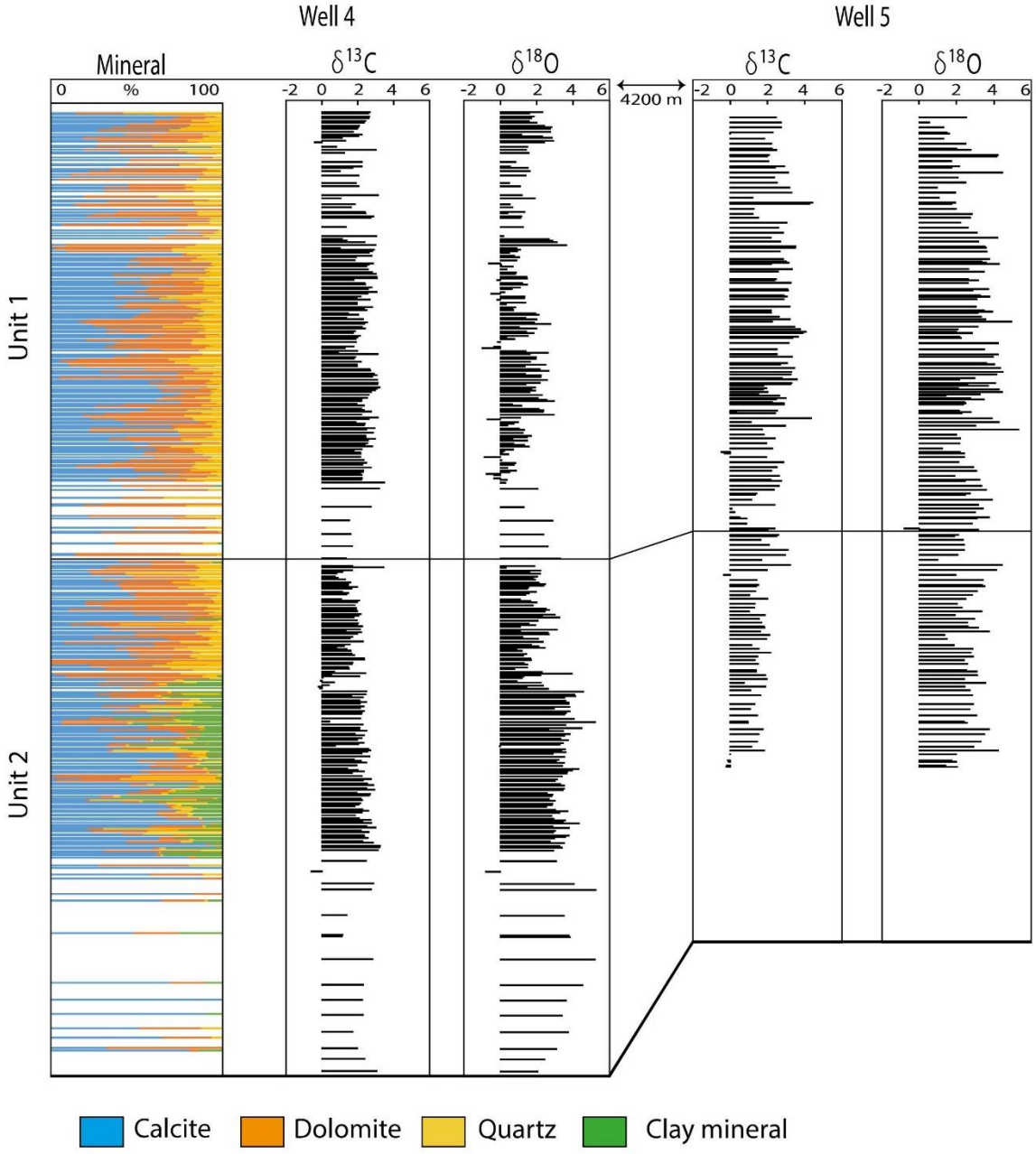


772

773 Figure 16 – Schematic transect showing profiles of bulk mineralogy, $\delta^{13}C$, $\delta^{18}O$ of the wells W4 and W5.
774 The well W5 does not have sufficient mineralogy data for correlation.

775

776

777

778

779

780 Table 4 - $\delta^{18}O$ and $\delta^{13}C$ (Avg.=average value, Q1=first quartile, Q3=third quartile) for each facies and
781 stratigraphic units (when available), for samples dominated by calcite and dolomite. Correlation
782 coefficients are calculated for each series when number of samples (n) are sufficient.

| | Name | n | d18O - Avg. | Q1 | Q3 | d13C - Avg. | Q1 | Q3 | Correl. coef. |
|---|---|---|---|---|---|---|---|---|---|
| CALCITE | SPH - UNIT 1 | 24 | 1.73 | 1.15 | 2.29 | 2.81 | 2.64 | 3.15 | -0.14 |
| | SPH - UNIT 2 | 12 | 2.53 | 2.07 | 3.02 | 2.40 | 2.00 | 2.79 | 0.65 |
| | SPH - UNIT 3 | 1 | -0.69 | -- | -- | 1.28 | -- | -- | -- |
| | STV - UNIT 2 | 1 | 1.69 | -- | -- | 1.56 | -- | -- | -- |
| | LAM - UNIT 1 | 10 | 1.67 | 1.04 | 2.99 | 2.63 | 2.25 | 3.19 | 0.34 |
| | SHR - UNIT 1 | 44 | 1.82 | 0.90 | 2.33 | 2.84 | 2.56 | 3.13 | -0.34 |
| | SHR - UNIT 2 | 13 | 2.16 | 1.90 | 3.09 | 2.28 | 2.09 | 2.85 | -0.02 |
| | SHR - UNIT 3 | 2 | -0.21 | -0.51 | 0.08 | 1.28 | 1.01 | 1.56 | -- |
| | GST-A - UNIT 1 | 11 | 0.66 | 0.71 | 1.09 | 2.65 | 2.42 | 3.03 | 0.26 |
| | GST-A - UNIT 2 | 2 | 2.04 | 1.73 | 2.35 | 2.80 | 2.75 | 2.85 | -- |
| | GST-A - UNIT 3 | 2 | -0.42 | -0.88 | 0.05 | 0.95 | 0.65 | 1.24 | -- |
| | GST-B - UNIT 2 | 2 | 1.63 | 1.24 | 2.02 | 2.48 | 2.17 | 2.79 | -- |
| | GST-C - UNIT 1 | 17 | 0.62 | 0.38 | 0.77 | 2.81 | 2.51 | 3.10 | 0.51 |
| | GST-C - UNIT 2 | 6 | 1.37 | 1.07 | 1.74 | 2.67 | 2.46 | 2.87 | -0.84 |
| DOLOMITE | SPH - UNIT 1 | 23 | 1.64 | 0.75 | 2.73 | 1.90 | 1.51 | 2.43 | 0.31 |
| | SPH - UNIT 2 | 7 | 3.28 | 2.88 | 3.60 | 1.55 | 1.39 | 1.94 | -0.21 |
| | STV - UNIT 1 | 12 | 0.49 | -0.15 | 1.29 | 1.42 | 1.22 | 1.86 | -0.13 |
| | STV - UNIT 2 | 2 | 3.03 | 2.64 | 3.43 | 1.84 | 1.84 | 1.85 | -- |
| | LAM - UNIT 1 | 15 | 0.99 | -0.42 | 2.43 | 1.99 | 1.16 | 2.69 | 0.66 |
| | LAM - UNIT 2 | 1 | 0.82 | -- | -- | 1.92 | -- | -- | -- |
| | SHR - UNIT 1 | 3 | 1.50 | 1.42 | 1.56 | 2.05 | 1.73 | 2.49 | -0.99 |
| | SHR - UNIT 2 | 2 | 2.54 | 2.25 | 2.82 | 0.50 | 0.07 | 0.93 | -- |
| | GST-A - UNIT 1 | 30 | 0.87 | 0.51 | 1.47 | 2.35 | 2.20 | 2.80 | 0.28 |
| | GST-A - UNIT 2 | 9 | 2.65 | 1.92 | 2.89 | 2.48 | 2.33 | 2.79 | 0.28 |
| | GST-A - UNIT 3 | 1 | -0.67 | -- | -- | -0.82 | -- | -- | -- |
| | GST-B - UNIT 1 | 5 | 0.17 | -0.86 | 0.88 | 2.42 | 2.16 | 2.31 | -0.62 |
| | GST-B - UNIT 2 | 5 | 0.67 | 0.36 | 0.86 | 1.77 | 1.86 | 2.38 | 0.89 |
| | GST-C - UNIT 1 | 35 | 0.96 | 0.58 | 1.38 | 2.72 | 2.53 | 2.90 | -0.16 |
| | GST-C - UNIT 2 | 21 | 2.57 | 1.84 | 3.00 | 2.64 | 2.27 | 2.84 | -0.11 |

783

784

785

786 ## 5 Interpretation and discussion

787 The BVF is mainly constituted by a limited mineral assemblage, composed essentially of calcite,
788 dolomite, silica, and Mg-clays. Different biological or chemical controls on mineral precipitation may
789 have exerted a strong influence on the diagenetic pathways of these sediments (Herlinger et al., 2017).
790 For example, the role of biological factors related to Mg-clays and dolomite precipitation has been

addressed by Burne et al. (2014), Pace et al. (2016), or Kirkham and Tucker (2018) both in the pre-salt formation or in other cases. Other studies considered part of the dolomite as a product of neomorphism of a microbially-influenced metastable precursor (Gomes et al., 2020) or formed within extracellular polymeric substances (EPS) (Sartorato, 2018). However, for other authors, the lack of direct textural or isotopic evidence for microbial deposits in most of the BVF, except for the uppermost meters of the formation, is evidence of dominant abiotic processes. The abiotic models emphasized not only the scarcity of microbial features but the role of Mg-clay as a source of elements, essentially for dolomite and silica precipitation (Wright and Barnett, 2015; Tosca and Wright, 2015; Farias et al., 2019). Although these processes have been extensively described and interpreted, very few papers (Wright and Barnett, 2020; Gomes et al., 2020; Carramal et al., 2022) have integrated a quantitative approach combined with spatial and stratigraphic distribution and elaborated on the relations between this distribution and the depositional or structural setting. This will be developed in the following discussion.

## 5.1 Syndepositional processes

### 5.1.1 Mg-clays

In our study area, Mg-clays are abundant, and rocks essentially constituted by them can reach 150 m in thickness in some wells, being in line with the extensive Mg-clay occurrences described in the West African and eastern Brazilian Margins (Wright and Barnett, 2015; Tosca and Wright, 2015; Saller et al., 2016; Sabato Ceraldi and Green, 2016; Herlinger et al., 2017; Farias et al., 2019; Lima and De Ros 2019; Gomes et al., 2020; Wright and Barnett, 2020). Moreover, the current Mg-clay content only represents a fraction of the original content, considering the extent of its replacement by microcrystalline and cryptocrystalline calcite, dolomite, and silica, as well as their dissolution (Herlinger et al., 2017; Lima and De Ros, 2019).

Jones and Gálan (1988) and Tosca and Wright (2015) suggested that the factors controlling the formation of Mg-rich clays are pH (alkalinity), $pCO_2$, and salinity; and that the specific chemical

conditions required for their precipitation could be achieved rapidly and with large lateral extensions through evaporative concentration. Biological materials, such as microbial cells or extracellular polymeric substances (EPS), could also act as substrates for Mg-silicate nucleation by lowering the interfacial energies for Mg-silicate precipitation (Tosca and Wright, 2015). The identification of Mg-clays in association with biofilms and microbial carbonate is reported in some works (Tosca et al., 2011; Burne et al., 2014; Perri et al., 2018).

In our case study, the facies with the highest preserved Mg-clay content (Mg-claystones with minor proportions of spherulites) occurs in Unit 2. Moreover, it seems that high $\delta^{18}O$ values measured on carbonates are associated with samples in which the highest Mg-clay content is found (i.e., well W4). The high isotopic values, both in $\delta^{13}C$ and $\delta^{18}O$ may suggest: 1) a lesser diagenetic alteration, as diagenesis would tend to decrease $\delta^{18}O$ values (Lima and De Ros, 2019); 2) evaporitic conditions (Talbot, 1990; Farias et al., 2019) and correlative evaporative concentrations of the water, also favoring Mg-clay precipitation and preservation (Pozo and Calvo, 2018; Galán and Pozo, 2011). Vertical partitioning is also observed for the clay mineralogy, with Mg-smectite dominant in Unit 3 passing upward to dominantly mixed layer kerolite/Mg-smectite and kerolite in Units 2 and 1. This Mg-clay distribution suggests a gradual change in the water chemistry as the genesis of the different types of Mg-clays is conditioned by variations in pH, salinity, and Si/Mg ratio (Jones and Gálan, 1988; Carramal et al., 2022; Netto et al., 2022). Netto et al. (2022) recognized a similar vertical trend of the Mg-clay minerals in samples from a well located in the Outer High structure of the Santos Basin. They interpreted the predominance of Mg-smectite (stevensite) in the lower part of the stratigraphic succession as due to early evaporative conditions while the precipitation of kerolite in the upper part would be related to the presence of relatively more diluted waters. Stevensite stability is favored by high salinity and pH and low to moderate Si/Mg ratios, while the kerolite stability is favored by moderate salinity, pH between 8 and 8.5, and low Si/Mg ratio, with transitions from one to the other represented by kerolite-stevensite interstratified minerals (Galan and Pozo, 2011). Tosca and Masterson (2014) even suggested a broader range of pH for kerolite formation, reaching higher values

of 9.4. In this case, the Si/Mg ratio would be one of the main factors for kerolite precipitation. According to these observations, the Mg-clays trend could indicate a variation in the detrital contribution in the basin, since kerolite formation is favored in environments with low detrital sediment input (Deocampo, 2015). This hypothesis is supported by the detrital grain abundance increase in Unit 3 and distribution of the grainstones with siliciclastic/volcanoclastic grains that are observed in Units 3 and 2, in the vicinity of the structural high, directly overlying the fractured substratum (explaining the abundance of volcanoclastic/siliciclastic material). The sources of solutes in the pre-salt lake are not evident, with potential sources including leaching and erosion of flood basalts outside the rift, enhanced by hydrothermal activity (Szatmari and Milani, 2016; Farias et al., 2019); intrabasinal magmatism (Szatmari et al., 2016; Wright, 2022); felsic rocks from the basement, in contact with groundwaters (Pietchz et al., 2018); marine seepage through the Walvis Ridge volcanic barrier (Farias et al., 2019); mantle exhumation and serpentinization (Tosca and Wright, 2015; Pinto et al. 2017; Lima et al., 2020). Despite the low proportion of terrigenous input in the basin, the higher contribution of detrital grains in Unit 3 and its progressive decrease indicates a change in the lake's water recharge pattern that could influence the Mg-clays type precipitation. A higher amount of non-magnesian clay minerals observed in laminites, intraclastic grainstones, and Mg-claystones with spherulites can also be associated with areas and periods characterized by higher detrital input.

From a spatial point of view, the facies with the largest preserved Mg-clay content predominate in lower areas, away from the structural high, and in relative lows within the high, as in the case of well W4. In these areas, Mg-clay occurs as very fine laminated fabrics, associated with a low amount of spherulites. On the contrary, the wells of transects A and B located on the structural high, as well as on its eastern flank (transect C), are characterized by very low content of Mg-clays, which occurs mainly as intraclasts and ooids. Such differences could be due to a system of different small and isolated lakes with no or only episodic lateral connection (Farias et al., 2019). However, the lateral continuity of the different seismic reflectors and stratigraphic units of the BVF (Wright and Barnett, 2017) point to a unique large lake, at least at field scale. Changes in hydrodynamic conditions are supported by the very

869 fine laminated fabrics deposited and well-preserved in low-energy environments, localized in lower
870 areas, and ooids associated with high-energy conditions, predominating in higher areas of the
871 depositional profile (Lima and De Ros, 2019; Basso et al., 2020; Carramal et al., 2022). The scarcity of
872 Mg-clays in these settings could also be related to lesser preservation and a stronger diagenetic
873 alteration, owing to variable physico-chemical conditions in such places. The high sensitivity of Mg-
874 clays to $pCO_2$ and pH, their high reactive surface area, and their Al-free composition can lead to their
875 destabilization, replacement, and dissolution during early diagenesis (Deocampo, 2005; Tosca, 2015;
876 Tosca and Wright, 2015).
877 Fluctuations in environmental conditions probably favored distinct Mg-clay minerals in time and
878 variable types and degrees of alterations (Carramal et al., 2022). The decrease of Mg-clays amounts in
879 the high areas of the depositional setting (and particularly in Unit 1) coincides with an increase of
880 dolomite and magnesite amounts, which suggest more intense replacement processes. The diagenetic
881 alterations of Mg-clays and their relationship with other minerals will be discussed below.
882

883 ### 5.1.2 Fascicular calcite crusts

884 Fascicular calcite crusts (or shrubs) from the Barra Velha and Macabu Formations have been illustrated
885 in several publications (Herlinger et al., 2017; Farias et al., 2019; Gomes et al., 2020; Lima and De Ros,
886 2020; Wright and Barnett, 2020) and are interpreted by these authors as products of abiotic
887 precipitation. According to Herlinger et al. (2017), the fascicular calcite aggregates are syngenetic
888 precipitates resulting from encrustation and replacement of other sediments, mainly stevensite.
889 Wright and Barnett (2015), Farias et al. (2019), and Lima and De Ros (2019), based on petrographic
890 characteristics, rather indicate a rapid vertical growth of crystals, directly at the sediment-water
891 interface or right below it, from highly carbonate-saturated solutions.
892 As the main constituent of the in-situ facies, the fascicular calcite crusts form mainly in transitional and
893 higher areas of the depositional profile. In higher sites, these carbonates are abundant, mostly devoid
894 of Mg-clays, and grew on top of each other. They may have formed directly at the water-sediment

895 interface as syngenetic precipitates (Lima and De Ros, 2019). In contrast, in lower areas of the studied
896 depositional profile, fascicular calcite crusts are mostly observed as incipient forms, being commonly
897 associated with spherulites and interstitial Mg-clays. In this case, the frequent engulfment of Mg-clays
898 in the calcite aggregates and their displacive crystal growth indicate that part of the shrubs precipitated
899 as a result of an early diagenetic process (Carramal et al., 2022), replacing and deforming the Mg-clays
900 (Lima and De Ros, 2019; Farias et al., 2019).
901 The preferential location of these crusts in shallow environments and the dominantly high $\delta^{13}C$ and
902 $\delta^{18}O$ isotopic values, observed for these carbonates in Units 2 and 1, suggest precipitation under the
903 influence of evaporative concentrations (Wright and Barnett, 2015; Sabato-Ceraldi and Green, 2016;
904 Barnett et al., 2018; Farias et al., 2019). For Saller et al. (2016), the morphology of these calcite crusts
905 is dependent on depositional energy, degree of supersaturation, and substrate. The development of
906 incipient forms in deeper and less energetic environments is in line with the previous observations of
907 Lima and De Ros (2019) or Basso et al. (2020), who also described "hybrid forms" between spherulites
908 and fascicular crusts. The interlayering between fascicular calcite crusts and intraclastic grainstones
909 point to rapid changes in hydrodynamic conditions. In the same way, the centimetric alternation of
910 fascicular calcite, spherulites, and Mg-clays observed in this study, seems to reflect local and rapid
911 changes in the lake chemistry and hydrodynamism (Gomes et al., 2020; Lima and De Ros, 2019;
912 Mercedes-Martín et al., 2019).
913 An alternative hypothesis based on sedimentological observations suggests that shrubby carbonate
914 formation might arise from the combination of changes in the hydrodynamic conditions and microbial
915 influence either in natural hot-spring deposits (Erthal et al., 2017) but also in anthropogenic
916 hyperalkaline, saline environments (Bastianini et al., 2019). Experimental data suggest that the
917 incipient formation of vertically stacking spherulitic calcite resembling pre-salt fascicular calcite habits
918 requires both the intervention of highly supersaturated waters and the presence of microbial-derived
919 polymers (Mercedes-Martín et al., 2021a, b). It was not possible to decipher such microbial influence
920 in our study.

At field scale, fascicular calcite crusts are observed in the three successive units, in quite similar proportions (Table 2), with a slight increase in Unit 1. They also gradually expand away from the structural high, from base to top of the succession (Fig. 4). This observation can be compared with the aggrading and subsequent prograding geometries with a gradual flattening outward geometry of clinoforms observed on seismic by Minzoni et al. (2020). They interpreted these features as a basinal shallowing-upward, with the filling of accommodation and the development of laterally extended, shallow high-energy settings. The moderate to high $\delta^{18}O$ values observed for fascicular calcite crusts in Units 2 and 1 are also suggestive of a progressive increase of the evaporitic conditions toward the end of the BVF deposition, which would lead to highly carbonate-saturated lake-waters. The rather constant $\delta^{13}C$ values compared to the larger range of $\delta^{18}O$ values (Fig. 16) indicates long water residence times in the paleolake, equilibrium between atmospheric and lake water $CO_2$, and evaporative conditions (Pietzsch et al., 2020).

## 5.2 Early diagenetic phases

Syngenetic and eogenetic processes occur in close association in the pre-salt deposits. The initial composition, constituted mainly by Mg-clays and fascicular calcite, is one of the factors influencing the diagenetic modifications and resulting products (Herlinger et al., 2017).

### 5.2.1 Spherulites and Mg-clay preservation

Spherulites are very common and abundant in the BVF, throughout the entire basin. The formation of calcite spherulites is a subject of discussion, having been interpreted as a result of: (1) biotic primary precipitation associated with microbial processes (Chafetz et al., 2018; Kirkham and Tucker, 2018), and (2) eodiagenetic products, replacing and/or displacing the laminated Mg-clays (Wright and Barnett, 2015, 2016; Herlinger et al., 2017; Lima and De Ros, 2019; Carramal et al., 2022).

In our study, spherulites appear in three sub-facies: Mg-claystones with low and with high proportions of spherulites; and grainstones. These facies are characterized at certain locations of the depositional

947 profile by moderate to intense dissolution of the clay matrix (Fig. 9F), generating porosity. This is in
948 line with the observations of Wright and Barnett (2020), who recognized three different associations
949 of spherulites in the BVF: 1) in association with Mg-clays; 2) with fenestral porosity, lacking Mg-clay;
950 and 3) as re-worked deposits. Moreover, the spherulites observed in our study frequently display
951 inclusions of Mg-clay, with a displacive growth that locally deformed the Mg-clay laminations. These
952 observations support a secondary diagenetic origin for the spherulites rather than primary syngenetic
953 precipitation. The similar $\delta^{13}C$ and $\delta^{18}O$ range of values than for fascicular calcite also indicate long
954 water residence times in the paleolake and evaporative conditions (Pietzsch et al., 2020).
955 The exact timing of spherulite formation relative to Mg-clay precipitation is also debated. Wright and
956 Barnett (2015, 2020) proposed the precipitation and deposition of an initial Mg-silicate gel, its
957 subsequent crystallization to different types of Mg-clay, in which the spherulites would grow and be
958 potentially re-worked. Based on the strong parallel orientation of the laminated deposits, on their
959 common association with siliciclastic particles and mud, and on the deformation of the Mg-clay
960 laminae by the very early precipitation of the spherulites, we interpreted that they precipitated within
961 an already formed Mg-clay fabric, following the work of Carramal et al. (2022). It must be noted that,
962 based on experimental observations, Mercedes-Martín et al. (2016) suggested that silicate gels might
963 not be required to encourage the formation of polycrystalline calcite grains which otherwise can be
964 the product of interference with organic acids.
965 The amounts of calcite spherulites, shrubs, and Mg-clays in the different facies are apparently
966 controlled by the intensity of the Mg-clay alteration processes in the higher and lower areas, related
967 to different hydrodynamic conditions and intensive dissolution processes. Indeed, we observe that the
968 transitional and higher areas of the depositional profile show low or absence of Mg-clays content and
969 a higher proportion of spherulites. In this setting, the dissolution of Mg-clays could be related to lake
970 level fluctuations, with rare potential subaerial exposure suggested by the flat-pebble breccia and
971 teepee structures observed in laminites facies, or to the dilution of lacustrine waters by meteoric influx
972 (Lima and De Ros, 2019; Carramal et al., 2022). Mg-clays dissolution is also important in the wells

973 located on the flank and in well W6, locations characterized by the presence of faults (Fig. 12). Such
974 areas would be more prone to $CO_2$ input by magmatic and hydrothermal activity (Herlinger et al., 2017;
975 Lima and De Ros, 2020) and to early diagenetic dissolution. Conversely, greater accumulation and
976 preservation of Mg-clays is observed in the northwest area, characterized by a lower structural position
977 and by rare faults.
978 Dissolution is a critical process of porosity generation in BVF deposits (Tosca and Wright, 2015),
979 especially in the Mg-claystones with spherulites, that originally presented a poor reservoir quality. In
980 addition, the Mg-clay dissolution could play a key role in later diagenesis (Tosca and Wright, 2015;
981 Carramal et al., 2022). The release into the system of $Mg^{2+}$, $SiO_2$ and minor $Na^+$ would favor the
982 precipitation of dolomite, silica, and Na-silicates (Tosca and Wright, 2015). This is supported by the
983 diagenetic features observed in the study area. The distribution of dissolution and dolomite in the Mg-
984 claystones share a similar increasing trend (Table 5) towards transitional and higher areas. In particular,
985 medium-crystalline mosaic dolomite is the most common dolomite fabric on the structural high, with
986 a maximum observed in Unit 1.

987 Table 5 – Statistical summary of the average and maximum amounts of Mg-clay, dolomite, and
988 secondary dissolution porosity in the Mg-claystones with spherulites.

| **Regions** | | **Lower** | | **Transitional** | | **Higher** | | **Flank (section C)** | |
|---|---|---|---|---|---|---|---|---|---|
| | | Average | Maximum | Average | Maximum | Average | Maximum | Average | Maximum |
| **Constituents (%)** | **Diagenetic phase** | | | | | | | | |
| **Mg-clay** | Syngenetic | 11.5 | 55.0 | 5.0 | 30.0 | 1.2 | 13.0 | 2.4 | 42.0 |
| **Dolomite** | Replacing constituents/Filling porosity | 17.5 | 70.0 | 34.0 | 88.0 | 27.0 | 80.0 | 31.0 | 83.0 |
| **Secondary dissolution porosity** | | 1.5 | 24.0 | 3.7 | 19.5 | 6.5 | 24.0 | 7.6 | 22.0 |

989
990
991
992
993
994
995
996

### 5.2.2 Dolomite

After the calcite spherulites and shrubs, dolomite is an important diagenetic mineral phase identified in the BVF sediments, occurring more as a replacement phase than as a pore-filling cement. The different fabrics observed can be associated with distinct timings.

The lamellar dolomites/magnesites, which mimic shapes of Mg-clays laminations plates are one of the specificities of the pre-salt sag deposits (Wright and Barnett, 2020; Carramal et al., 2022). These lamellar aggregates were associated with highly evaporative conditions, as attested by the presence of magnesite, which requires highly concentrated waters (Farias et al., 2019). Carramal et al. (2022) suggested that they initially formed filling shrinkage pores generated by Mg-clays dehydration or by its replacement by kerolite. The well-expressed pseudomorphosis of the Mg-clay laminae suggests very early diagenesis prior to any significant compaction that would have closed the shrinkage porosity.

Another recurrent form of dolomite is the microcrystalline dolomite, occurring mainly in the transition zones and Unit 1, largely associated with laminites facies. It is often observed as a replacement of Mg-clays and commonly occurs in association with crypto- to fine crystalline calcite. Dolomite samples of the laminites facies show lower ranges of $\delta^{18}O$ and $\delta^{13}C$ values, compared to calcites sampled in the same facies and to dolomites sampled in other facies. This may point to episodic changing environmental conditions and more diluted waters, leading to Mg-clays replacement. In our case study, the microcrystalline dolomite is precisely observed in the uppermost part of the BVF, and associated with crenulated laminites, generally interpreted as microbial in origin (Sartorato, 2018; Artagão, 2018). Given these two points, the role of biological processes in its formation cannot be totally discarded.

The rhombohedral dolomite is predominantly found associated with fascicular calcite crusts and spherulites, often “floating” in the interstitial space among the calcite shrubs and spherulites. This dolomite fabric concentrates mainly in lower areas and Unit 2, reflecting their close association with Mg-clays. In their depositional model for the BVF, Farias et al. (2019) proposed an alternative model for the formation of dolomite rhombs. According to them, the beginning of the evaporation process

would result in precipitation of fascicular calcite at the sediment-water interface and precipitation of rhombohedral dolomites at the brine-air interface, which would then accumulate at the bottom of the saline lake. With progressive evaporation of the $CaCO_3$-rich waters increasing the Mg/Ca ratio into the systems, the dolomitization of the Mg-clay matrix occurred (Farias et al. 2019). This would result in the deposition of levels of fascicular calcite crusts alternated with levels of dolomite rhombs, and not in the observed distribution of rhombs "floating" in the interstitial spaces among shrubs. Moreover, this would not explain the dolomite distribution associated with the spherulites. Finally, in these facies, the isotopic values observed for dolomite show a similar range of $\delta^{18}O$ values but lower $\delta^{13}C$ values compared to calcite of the same facies, which is not the expected behavior for a continuous increasing evaporation of the lake waters. Given these observations, the rhombohedral dolomite likely results from the partial replacement of Mg-clays before their subsequent dissolution (Herlinger et al., 2017).

### 5.2.2 Silica

Early diagenetic silica occurs mainly as nodules (Fig. 3G), layers, and pervasive microcrystalline quartz. Despite the limited amounts of silica observed in the petrographic descriptions, it is more common in Unit 1, where it is a relevant component in XRD analyses (Fig. 16).

The origins and timing of silica in the BVF are debated. Various forms of silica have been identified in the pre-salt formations of the conjugate South Atlantic margins, in Brazil (offshore Santos and Campos Basins) and Angola (Kwanza and Namibe Basins). In the Kwanza Basin, the original carbonate deposits suffered important diagenesis where silica metasomatism plays a key role with: 1) early replacement and cementation by silica at relatively low temperature (< 100°C); 2) a second silica generation linked to high-temperature hydrothermal processes (Tritlla et al., 2018; Teboul et al., 2019). In the Campos Basin (Pão de Açúcar), pervasive silicification of the original carbonates attributed to a late hydrothermalism phase, that generated corrosion, porosity formation, and silica replacement and precipitation (Vieira de Luca et al., 2017). Finally, eogenetic silica precipitation has been interpreted as

Mg-clays replacement (Lima and De Ros, 2019; Wright and Barnett, 2020), linked to freshening lake periods when relatively lower alkalinity values would favor its precipitation (Wright and Barnett, 2020). The higher proportions of silica in Unit 1 (and especially within laminites) associated with the presence of replacive microcrystalline dolomite or calcite and their respective isotopic signatures (see above) also suggest the alternation of freshening-evaporation lake conditions (Wright, 2022) or reduced infiltration to sub-bottom aquifers (Mercedes-Martín et al., 2019). Alternatively, a hypothesis of precipitation as a syngenetic phase is addressed in Sartorato et al. (2020), with the cryptocrystalline silica resulting from organo-mineralization processes. However, in the study area, this silica phase is rarely found.

### 5.3 Mesogenetic phases and hydrothermal processes

In our case study, the higher areas and southeast flank show a significant dolomitization process, evidenced by the increase of pervasive mosaic dolomite, especially within in-situ facies (Mg-claystones with spherulites, laminites, and fascicular calcite crusts). The higher occurrence of dolomite associated with a decrease in the amount of Mg-clay may again suggest the replacement of Mg-clay by dolomite. However, petrographic observations (i.e., Fig. 7E – 7H) showed that the granular mosaic dolomite can also replace pervasively fascicular calcites and spherulites, grow as a pore-filling cement in the primary porosity (mostly associated with grainstones) or also co-occur with macrocrystalline quartz as fracture-infill. This indicates a late eogenetic to mesogenetic timing.

Total replacement of the original carbonate fabrics is frequently observed. Moreover, intervals with macrocrystalline quartz and coarse blocky calcite cement, are recurrent. The depositional texture exerted a strong control on the diagenetic modifications (Herlinger et al., 2017). Grainstones and fascicular calcite crusts exhibit heterogeneous cementation, and more dissolution features, as the initial porous systems of these sediments may have facilitated fluid circulation. As faults are more common in those areas, the structural pattern apparently acted as a major controlling factor. The

greater intensity of such diagenetic alterations, as well as the presence of saddle dolomite, could be related to the circulation of hydrothermal fluids along those fractured zones.

However, extensive hydrothermal processes, like those reported in other portions of the Santos and Campos Basin (Vieira de Luca et al., 2017; Lima et al., 2020), were not found in the study area. Silicification has no peculiar spatial distribution and does not exhibit features indicative of hydrothermal events, as described in the coeval succession of the Pão de Açucar area of Campos Basin (Vieira de Luca et al., 2017), or the Parque das Baleias area of Northern Campos Basin (Lima et al., 2020). Isotopic ratios do not point either to an important hydrothermalism diagenetic overprint, given the relatively high and positive values. Mineral phases such as macrocrystalline calcite, saddle dolomite, barite, celestine and fluorite, characteristic of hydrothermal alteration of the pre-salt formation in the Campos Basin (Lima and De Ros, 2020), have been only observed in a very low proportion in the study area. The QEMSCAM and XRD analyses also show that these minerals occur only as minor or even trace amounts. Among the mentioned minerals, saddle dolomite is the most prominent, and although it is not by itself indicative of hydrothermal processes, it is often associated with wells located in fault zones, suggesting hydrothermal influence (Herlinger et al., 2017). Hydrothermal activity contributed only locally to the alteration of the pre-salt carbonates and to the precipitation of specific mineral assemblages.

## 6 Conclusions

- The integrated analysis of sedimentary facies, geochemistry data, and diagenetic features of the BVF in a key area of the Santos Basin highlighted the roles of depositional setting and primary constituents on the diagenetic processes. The quantitative characterization of diagenetic products allowed to recognize spatial and stratigraphic trends of syngenetic and diagenetic phases, indicating the Mg-clays as an initial substrate.

- The pattern of Mg-clays preservation indicates that the structural setting was a strong determinant of the diagenetic changes, with stronger diagenetic alterations along structural highs and fault zones.
- The precipitation of fascicular calcite was much more developed in higher areas, and their alternation with Mg-clay precipitates suggests local fluctuations of evaporative conditions of the basin. The gradual lateral expansion of fascicular calcite away from the structural high during Unit 1 is associated with a large-scale basinal shallowing upward trend.
- The data from the present study suggest that evaporative conditions prevailed in the Aptian pre-salt succession with some fluctuations in environmental conditions favoring different Mg-clay minerals in time, distinct isotopic signatures, and variable types and degrees of diagenetic alterations. In Unit 3 (base), low isotopic ratios, higher detrital siliciclastic/volcanoclastic grains, and dominance of Mg-smectite suggest relatively dilute waters, with high detrital input and low to moderate Si/Mg ratios. In Unit 2, the high isotopic values, the progressive increase of mixed layer kerolite/Mg-smectite and kerolite, the decrease of detrital grains (apart from the structural high) are indicators of more evaporative conditions and lesser input of water. Finally, in Unit 1 (top), lower $\delta^{18}O$ values but high $\delta^{13}C$, the dominance of kerolite, the occurrence of silica and dolomitic replacement phases may point to evaporative conditions but with frequent fluctuations and freshening of the water, explaining the stronger diagenetic imprint.
- Dolomite is one of the most relevant diagenetic phases in the BVF, largely associated with Mg-clays replacement, developing in several fabrics. Lamellar dolomite/magnesite aggregates, microcrystalline and rhombohedral dolomite are early diagenetic phases, strongly dependent on the environmental conditions and variations of the lake water composition. Given its pervasive aspect and its co-occurrence with macrocrystalline quartz as fracture-infill, mosaic dolomite is a mesogenetic product. Its preferential occurrence in higher structural positions and flank regions may suggest a structural control.

- The dissolution features indicate an important process of secondary porosity generation, mainly associated with diagenetic Mg-clays destabilization.
- The presence of macrocrystalline calcite, saddle dolomite, barite, celestine and fluorite are typical products of hydrothermal alteration. Their distribution in the higher structural positions and in the southeast flank may be related to minor hydrothermal fluids circulation, also having an impact on the alteration of carbonate phases.


## Acknowledgments

The results and interpretations of this paper are part of the Ph.D. funded by Petroleo Brasileiro S.A. – Petrobras. The authors greatly acknowledge Petrobras for the data release and permission to publish this research. We are grateful for the analytical work provided by Petrobras Research Center (CENPES), and we also thank Camila Wense Ramnani and Daniel M. Oliveira for their valuable contributions. The authors wish also to thank reviewers L. F. De Ros, R. Mercedes-Martín, and R. Swennen, as well as the Editor Dr. Miroslaw Slowakiewicz for their constructive suggestions that greatly improve the quality of the manuscript.

## 7 References


Almeida, F.F.M., Hasui, Y, Brito Neves, B.B., Fuck, R.A., 1981. Brazilian structural provinces: an introduction. Earth-Science Reviews. V. 17, n. 1-2, p. 1–29.

Alves, T.M., Fetter, M., Lima, C., Cartwright, J.A., Cosgrove, J., Gang, A., Queiroz, C.L., Strugale, M., 2017. An incomplete correlation between pre-salt topography, top reservoir erosion, and salt deformation in deep-water Santos Basin (SE Brazil), Marine and Petroleum Geology 79, p300-320.

Artagão, V.M., 2018. Análise estratigráfica de alta resolução aplicada aos depósitos da Formação Barra Velha, Bacia de Santos : identificação, correlação e mecanismos de contrôle de ciclos sedimentares. Master thesis. UERJ, Brasil (in Portuguese).

Asmus, H., Ponte, F., 1973. The Brazilian marginal basins, in The South Atlantic Springer, New York, pp. 87-133.

Barnett A.J., Obermaier, M., Amthor, J., Juk, K., Camara, R., Sharafodin, M., Bolton, M., 2018. Origin and significance of thick carbonate grainstone packages in non-marine successions: a case study from the Barra Velha Formation, Santos Basin. AAPG Search and Discovery Article #11116, adapted from poster presentation, AAPG Annual Convention and Exhibition, Salt Lake City, Utah, 20–23.

Basso, M., Belila, A.M.P., Chinelatto, G.F., Souza, J.P.P., Vidal, A.C., 2020. Sedimentology and petrophysical analysis of pre-salt lacustrine carbonate reservoir from the Santos Basin, southeast Brazil. Int J Earth Sci (Geol Rundsch).

Bastianini, L., Rogerson, M., Mercedes-Martín, R., Prior, T. J., Cesar, E. A., Mayes, W. M., 2019. What Causes Carbonates to Form “Shrubby” Morphologies? An Anthropocene Limestone Case Study. Frontiers in Earth Science, 7(September), 1–19.

Burne R. V., Moore L. S., Christy A. G., Troitzsch U., King P. L., Carnerup A. M., Hamilton P. J., 2014. Stevensite in the modern thrombolites of Lake Clifton, Western Australia: a missing link in microbialite mineralisation? Geology 42, 575– 578.

Cainelli, C., Mohriak, W.U., 1999. Some remarks on the evolution of sedimentary basins along the Eastern Brazilian continental margin: Episodes, v. 22, p. 206–216.

Carlotto, M.A., Silva, R.C.B., Yamato, A.A., Trindade, W.L., Moreira, J.L.P., Fernandes, R.A.R., Ribeiro, O.J.S., 2017. Libra: A Newborn Giant in the Brazilian Pre-salt Province. In: R. K. Merrill and C. A. Sternbach (Eds). Giant fields of the decade 2000–2010. Houston, Texas, AAPG Memoir 113. P. 165–176.

Carminatti, M., Wolff, B., Gamboa, L., 2008. New exploratory frontiers in Brazil. In: 19th World Petroleum Congress, vol. 19, Congress Paper, Madrid.

Carminatti, M., Dias, J.L., Wolff, B., 2009. From turbidites to carbonates: breaking paradigms in deep waters: Houston, Texas, Offshore Technology Conference, 4–7 May, OTC 20124.

Carramal, N.G, Oliveira, D.N., Cacela, A.S.M, Cuglieri M.A.A, Natasha, P. Rocha N.P., Viana, S.M., Toledo, S.L.V, Pedrinha, S., De Ros, L.F., 2022. Paleoenvironmental Insights from the Deposition and

1184 Diagenesis of Aptian Pre-Salt Magnesium Silicates from Lula Field, Santos Basin, Brazil. Journal of
1185 Sedimentary Research, v. 92, p. 12–31.

1186 Chaboureau, A. C., Guillocheau, F., Robin, C., Rohais, S., Moulin, M., Aslanian, D., 2012.
1187 Palaeogeographic evolution of the central segment of the South Atlantic during Early Cretaceous times:
1188 palaeotopographic and geodynamic implications. Tectonophysics, 14, 6489.

1189 Chafetz, H.S., Barth, J., Cook, M., Guo, X., Zhou, J., 2018. Origins of carbonate spherulites: implications
1190 for Brazilian Aptian Pre-Salt reservoir. Sediment. Geol. 365, 21–33.

1191 Chang, H.K., Kowsmann, R.O., Figueiredo, A.M.F., Bender, A., 1992. Tectonics and stratigraphy of the
1192 East Brazil Rift system: an overview. Tectonophysics 213 (1), 97-138.

1193 Conceição, J.C., Zalan, P.V., Wolff, S., 1988. Mecanismo, evolução e cronologia do rift Sul-Atlantico.
1194 Bol. Geocienc. Petrobras, 2: 255-265.

1195 Deocampo D.M., 2005. Evaporative evolution of surface waters and the role of aqueous $CO_2$ in
1196 magnesium silicate precipitation: Lake Eyasi and Ngorongoro crater, northern Tanzania. South African
1197 J. Geol. 108, 493–504.

1198 Deocampo, D.M., 2015, Authigenic clay minerals in lacustrine mudstones, in Geological Society of
1199 America Special Paper 515, p. 49–64.

1200 Deschamps, R., Rohais, S., Hamon, Y., Gasparrini, M., 2020. Dynamic of a lacustrine sedimentary
1201 system during late rifting at the Cretaceous–Palaeocene transition: Example of the Yacoraite
1202 Formation, Salta Basin, Argentina. The depositional record 6:490–523.

1203 Dias, J., Oliveira, J., Vieira, J., 1988. Sedimentological and stratigraphyc analysis of the Lagoa Feia
1204 Formation, rift phase of Campos basin, offshore Brazil. Rev. Bras. De Geociências 18, 252–260.

1205 Dias, J.L., 2005, Tectônica, estratigrafia e sedimentação no Andar Aptiano da margem leste brasileira :
1206 Boletim de Geociências da Petrobras, v. 13, p. 7–25.

1207 Dickson, J.A.D., 1965, A modified staining technique for carbonates in thin section: Nature, v. 205, p.
1208 587.

1209 Erthal, M. M., Capezzuoli, E., Mancini, A., Claes, H., Soete, J., Swennen, R., 2017. Shrub morpho-types
1210 as indicator for the water flow energy – Tivoli travertine case (Central Italy). Sedimentary Geology, 347,
1211 79–99.

1212 Farias, F., Szatmari, P., Bahniuk, A., França, A. B., 2019. Evaporitic carbonates in the pre-salt of Santos
1213 Basin – Genesis and tectonic implications. Marine and Petroleum Geology, 105, 251-272.

1214 Galán, E., Pozo, M., 2011. Palygorskite and sepiolite deposits in continental environments. Description,
1215 genetic patterns and sedimentary settings. In: Developments in Clay Science. Vol. 3, Elsevier, pp. 125–
1216 173

1217 Gomes, P.O., Kilsdonk, B., Minken, J., Grow, T., Barragan, R., 2009. The Outer High of the Santos Basin,
1218 southern São Paulo Plateau, Brazil: pre-salt exploration outbreak, paleogeographic setting, and
1219 evolution of the syn-rift structures. In: AAPG Search and Discovery Article #10193.

Gomes, J.P., Bunevich, R.B., Tedeschi, L.R., Tucker, M.E., Whitaker, F.F., 2020. Facies classification and patterns of lacustrine carbonate deposition of the Barra Velha Formation, Santos Basin, Brazilian Pre-salt, Marine and Petroleum Geology, Volume 113.

Heilbron, M.L., Pedrosa-Soares, A.C., Campos Neto, M.C., Silva, L.C., Trouw, R.A.J., 2004. Província Mantiqueira. In: V.M. Mantesso-Neto, A. Bartorelli, C.D.R. Carneiro, Brito Neves, B.B. (orgs.). Geologia do Continente Sul-Americano. São Paulo, Editora Beca, p. 203-234.

Herlinger, R. J, Zambonato, E.E., De Ros, L.F., 2017, Influence of Diagenesis on the Quality of Lower Cretaceous Pre-Salt Lacustrine Carbonate Reservoirs from Northern Campos Basin, Offshore Brazil: Journal of Sedimentary Research, v. 87, p. 1285–1313.

Jones, B. F., Galan, E., 1988. Sepiolite and Palygorskite. In: Bailey, S. W. (ed.) Hydrous Phyllosilicates, Reviews in Mineralogy, 19. Mineralogical Society of America, Washington, DC, 631–674.

Karner, G.D., Driscoll, N.W., Barker, D.H.N., 2003. Synrift subsidence across the West African continental margin: The role of lower plate ductile extension. In: Arthur, T.J., MacGregor, D.S., Cameron, N.R. (Eds.), Petroleum Geology of Africa: New Themes and Developing Technologies. Geol. Soc. Spec. Publ Vol. 207, pp. 105–125.

Karner, G. D., Gamboa, L. a. P., 2007. Timing and origin of the South Atlantic pre-salt sag basins and their capping evaporites. Geological Society, London, Special Publications, 285(1), 15–35.

Kirkham, A., Tucker, M.E., 2018. Thrombolites, spherulites and fibrous crusts (Holkerian, Purbeckian, Aptian): context, fabrics and origins. Sediment. Geol. 374, 69–84.

Lentini, M. R., Fraser, S. I., Sumner, H. S., Davies, R. J., 2010. Geodynamics of the central South Atlantic conjugate margins: implications for hydrocarbon potential. Petroleum Geoscience, 16.

Liechoscki de Paula Faria, D., Tadeu dos Reis, A., Gomes de Souza, O. Jr., 2017. Three-dimensional stratigraphic-sedimentological forward modelling of an Aptian carbonate reservoir deposited during the sag stage in the Santos basin, Brazil. Marine and Petroleum Geology, 88, 676-695.

Lima, B.E., De Ros, L.F., 2019. Deposition, diagenetic and hydrothermal processes in the Aptian Pre-Salt lacustrine carbonate reservoirs of the northern Campos Basin, offshore Brazil. Sediment. Geol. 383, 55–81.

Lima, B. E., Tedeschi, L. R., Pestilho, A. L. S., Santos, R. V., Vasquez, J. C., Guzzo, J. V. P., De Ros, L. F., 2020. Deep-burial hydrothermal alteration of the Pre-Salt carbonate reservoirs from northern Campos Basin, offshore Brazil: Evidence from petrography, fluid inclusions, Sr, C and O isotopes. Marine and Petroleum Geology, 113.

Magalhaes, A.J.C., Raja Gabaglia, G.P., Fragoso, D.G.C., Bento Freire, E., Lykawka, R. Arregui, C.D. Silveira, M.M.L. Carpio, K.M.T., De Gasperi A., Pedrinha, S., Artagao, V.M., Terra, G.J.S., Bunevich, R.B., Roemers-Oliveira, E., Gomes, J.P., Hernandez, J.I., Hernandez, R.M., Bruhn, C.H.L., 2020. High-resolution sequence stratigraphy applied to reservoir zonation and characterisation, and its impact on production performance – shallow marine, fluvial downstream, and lacustrine carbonate settings. Earth-Science Reviews, 210

Mercedes-Martín, R., Ayora, C., Tritlla, J., Sánchez-Román, M., 2019. The hydrochemical evolution of alkaline volcanic lakes: a model to understand the South Atlantic Pre-salt mineral assemblages. Earth-Science Reviews, 198, 102938.

Mercedes-Martín, R., Brasier, A.T., Rogerson, M.R., Reijmer, J.J.G., Vonhof, H.B., Pedley, H.M., 2017. A depositional model for spherulitic carbonates associated with alkaline, volcanic lakes. Mar. Pet. Geol. 86, 168–191.

Mercedes-Martín, R., Rao, A., Rogerson, M., & Sánchez-Román, M., 2021a. Effects of Salinity, Organic Acids and Alkalinity in the Growth of Calcite Spherulites: Implications for Evaporitic Lacustrine Sedimentation. The Depositional Record, (December 2020), 1–22.

Mercedes-Martín, R., Rogerson, M.R., Brasier, A.T., Vonhof, H.B., Prior, T.J., Fellows, S.M., Reijmer, J.J.G., Billing, I., Pedley, H.M., 2016. Growing spherulitic calcite grains in saline, hyperalkaline lakes: experimental evaluation of the effects of Mg-clays and organic acids. Sedimentary Geology, 335, 93-102.

Mercedes-Martín, R., Rogerson, M., Prior, T. J., Brasier, A. T., Reijmer, J. J. G., Billing, I., Pedley, M., 2021b. Towards a morphology diagram for terrestrial carbonates: Evaluating the impact of carbonate supersaturation and alginic acid in calcite precipitate morphology. Geochimica et Cosmochimica Acta, 306, 340–361.

Milani, E.J., Rangel, H.D., Bueno, G.V., Stica, J.M., Winter, W.R., Caixeta, J.M., Neto, O.C.P, 2007. Bacias sedimentares brasileiras : Cartas estratigráficas – Introdução. Boletim de Geociências da Petrobras, 15(2), p. 183-198.

Minzoni, M., Cantelli, A., Thorton, J., Wignall, B., 2021. Seismic-Scale Geometries and Sequence-Stratigraphic Architecture of Early Cretaceous Syn-Post Rift Carbonate Systems, Presalt Section, Brazil. Geological Society, London, Special Publications, 509, 105-126

Mio, E.D., 2005. Modelagem crustal da Bacia de Santos pela integraçao de metodos geofísicos, 94 pp. Thesis (Master). Instituto de Geociências da Universidade Estadual Paulista, Rio Claro, São Paulo.

Morad, S., Al-Aasm, I. S., Nader, F. H., Ceriani, A., Gasparrini, M., Mansurbeg, H., 2012. Impact of diagenesis on the spatial and temporal distribution of reservoir quality in the Jurassic Arab D and C Members, offshore Abu Dhabi oilfield, United Arab Emirates. GeoArabia, 17, 17–56.

Moreira, J. L. P., Madeira, C. V., Gil, J. A., Machado, M.A.P., 2007, Bacia de Santos: Boletim de Geociências da Petrobras, v. 15 (2), p. 531-549.

Moulin, M., Aslanian, D., Unternehr, P., 2010. A new starting point for the history of the Equatorial and South Atlantic. Earth-Science Reviews 98, p. 1–37.

Muniz, M.C., Bosence, D.W.J., 2015, Pre-salt microbialites from the Campos Basin (offshore Brazil): image log facies, facies model and cyclicity in lacustrine carbonates, in Bosence, D.W.J., Gibbons, K.A., Le Heron, D.P., Morgan, W.A., Pritchard, T., and Vining, B.A., eds., Microbial Carbonates in Space and Time: Implications for Global Exploration and Production: Geological Society of London, Special Publication, 418, p. 221–242.

Netto, P.R.A., Pozo, M., da Silva, M.D., Mexias, A.S., Gomes, M.E.B., Borghi, L., Rios-Netto, A.M., 2022. Authigenic Mg-clay assemblages in the Barra Velha Formation (Upper Cretaceous) from Santos Basin (Brazil): The role of syngenetic and diagenetic process, Applied Clay Science 216.

Pace A., Bourillot R., Bouton A., Vennin E., Galaup S., Bundeleva I., Patrier P., Dupraz C., Thomazo C., Sansjofre P., Yokoyama Y., Franceschi M., Anguy Y., Pigot L., Virgone A., Visscher P.T. 2016. Microbial and diagenetic steps leading to the mineralisation of Great Salt Lake microbialites. Sci. Rep. 6, 31495.

Papaterra, G.E.Z., 2010. Pré-sal: Conceituação Geológica sobre uma Nova Fronteira Exploratória no Brasil. Rio de Janeiro. Master thesis. UFRJ, Brasil (in Portuguese).

Pereira, M.J., Feijó, F.J., 1994. Bacia de Santos. Estratigrafia das Bacias Sedimentares do Brasil. Boletim de Geociências da Petrobras, 8, p. 219-234.

Perri, E., Tucker, M.E., Słowakiewicz, M., Whitaker, F., Bowen, L. and Perrotta, I.D., 2018. Carbonate and silicate biomineralization in a hypersaline microbial mat (Mesaieed sabkha, Qatar): Roles of bacteria, extracellular polymeric substances and viruses. Sedimentology, 65: 1213-1245.

Pietzsch, R., Oliveira, D.M., Tedeschi, L.R., Neto, J.V.Q., Figueiredo, M.F., Vazquez, J.C., de Souza, R.S., 2018. Palaeohydrology of the lower cretaceous pre-salt lacustrine system, from rift to post-rift phase, Santos Basin, Brazil. Palaeogeogr. Palaeoclimatol. Palaeoecol. 507, 60–80.

Pietzsch, R., Tedeschi, L. R., Oliveira D. M., Anjos, C. W. D. Vazqueza, J. C., Figueiredo, M. F., 2020. Environmental conditions of deposition of the Lower Cretaceous lacustrine carbonates of the Barra Velha Formation, Santos Basin (Brazil), based on stable carbon and oxygen isotopes: A continental record of pCO2 during the onset of the Oceanic Anoxic Event 1a (OAE 1a) interval?, Chemical Geology, Volume 535.

Pinto, V.H.G., Manatschal, G., Karpoff, A.M., Ulrich, M. and Viana, A.R., 2017. Seawater storage and element transfer associated with mantle serpentinization in magma-poor rifted margins: A quantitative approach. Earth Planet Sci. Lett., 459, 227–237.

Popoff, M., 1988. Du Gondwana à l'Atlantique sud : les connections du fossé de la Bénoué avec les bassins du Nord-Est bresilien jusqu'à l'ouverture du golfe de Guinée au Crétacé inférieur. Journal of African Earth Sciences Special Publication 7, 2: 409-431.

Pozo, M., Calvo, J.P., 2018. An overview of authigenic magnesian clays. Minerals 8 (520), 1–22.

Rabinowitz, P.D., Labrecque, J., 1979, The Mesozoic South Atlantic Ocean and evolution of its continental margins: Journal of Geophysical Research, v. 84, 5973– 6002.

Rezende, M.F., & Pope, M.C. 2015. Importance of depositional texture in pore characterization of subsalt microbialite carbonates, offshore Brazil. Geological Society, London, Special Publications, 418(1), 193–207. https://doi.org/10.1144/SP418.2

Rodriguez-Carvajal, J. and Roisnel, T. 1998. FullProf.98 and WinPLOTR: New Windows 95/NT Applications for Diffraction. Commission for Power Diffraction, International Union for Crystallography. Newsletter N°20 (May-August).

Sabato-Ceraldi, T., Green, D., 2016. Evolution of the South Atlantic Lacustrine deposits in response to Early Cretaceous rifting, subsidence and lake hydrology. In: Sabato Ceraldi, T., Hodgkinson, R.A., Backe, G. (Eds.), Petroleum Geoscience of the West African Margin. Geological Society, London, Special Publications, pp. 438.

Saller, A., Rushton, S., Buambua, L., Inman, K., McNeil, R., Dickson, J.T., 2016. Presalt stratigraphy and depositional systems in the Kwanza Basin, offshore Angola. AAPG (Am. Assoc. Pet. Geol.) Bull. 100 (7), 1135–1164.

Sartorato, A.C.L., 2018. Caracterização faciológica, estratigráfica e diagenética dos reservatórios carbonáticos da Formação Barra Velha, Bacia de Santos. Master thesis. UERJ, Brazil (in portuguese).

Sartorato, A.C.N., Tonietto, S.N., Pereira, E. 2020. Silicification and dissolution features in the brazilian Pre-salt Barra Velha formation: impacts in the reservoir quality and insights for 3D geological modeling. Rio Oil & Gas Expo and Conference.

Szatmari, P., Milani, E.J., 2016. Tectonic control of the oil-rich large igneous carbonate-salt province of the South Atlantic rift. Mar. Petrol. Geol. 77, 567-596.

Talbot, M.R., 1990. A review of the palaeohydrological interpretation of carbon and oxygen isotopic ratios in primary lacustrine carbonates. Chem. Geol. Isot. Geosci. 80 (4), 261–279 Amsterdam.

Tanaka, A.P., Faria, D.L.P., Gomes, J.P.B., Souza Jr., O.G., 2018. Geological characterisation and modeling of an Aptian carbonate reservoir in the Santos basin, Brazil. In: AAPG 2018 AAPG Annual Convention and Exhibition, Salt Lake City, Utah, May 20–23.

Taylor, J.M., 1950. Pore space reduction in sandstone. Bulletin of the American Association of Petroleum Geologists 34, 701–716.

Teboul, P.A., Durlet, C., Girard, J.P., Dubois, L., San Miguel, G., Virgone, A., Camoin, G., 2019. Diversity and origin of quartz cements in continental carbonates: example from the Lower Cretaceous rift deposits of the South Atlantic margin. Appl. Geochem., 100, 22–41.

Tedeschi, L.R., 2017. Doctor of Philosophy Thesis In: Lower Cretaceous Climate Records and the Correlation Between Marine and Lacustrine Settings (Europe and South America). University of Oxford.

Terra, G.J.S., Spadini, A.R., Franca, A.B., Sombra, C.L., Zambonato, E.E., Juschaks, L.C.S., Arienti, L.M., Erthal, M.M., Blauth, M., Franco, M.P., Matsuda, N.S., Da Silva, N.G.C., Moretti Jr., P.A., D'Avila, R.S.F., De Souza, R.S., Tonietto, S.N., Dos Anjos, S.M.C., Campinho, V.S., Winter, W.R., 2010. Classificação de rochas carbonáticas aplicável ás bacias sedimentares brasileiras. Bol. Geociencias Petrobras 18, 9–29.

Terry, R.D., and Chilingar, G.V., 1955. Summary of ‘‘concerning some additional aids in studying sedimentary formations’’ by M.S. Shvetsov: Journal of Sedimentary Petrology, v. 25, 229–234.

Torsvik, T.H., Rousse, S., Labails, C., Smethurst, M.A., 2009. A new scheme for the opening of the South Atlantic Ocean and the dissection of an Aptian salt basin. Geophysical Journal International.

Tosca, N.J., Macdonald, F.A., Strauss, J.V., Johnston, D.T., and Knoll, A.H., 2011. Sedimentary talc in Neoproterozoic carbonate successions. Earth and Planetary Science Letters, 306 (1), 11–22.

Tosca, N., 2015. Geochemical pathways to Mg-silicate formation. In: Pozo, M., Gal´an, E. (Eds.), Magnesian Clays: Characterization, Origin and Applications, pp. 283–329. AIPEA Educational Series, Pub. No 2, Digilabs, Bari, Italy.

Tosca, N.J., Masterson, A.L., 2014. Chemical controls on incipient Mg-silicate crystallisation at 258C: implications for early and late diagenesis: Clay Minerals, v. 49, p. 165–194.

Tosca, N.J., Wright, V.P., 2015. Diagenetic Pathways Linked to Labile Mg-Clays in Lacustrine Carbonate Reservoirs: a Model for the Origin of Secondary Porosity in the Cretaceous Pre-salt Barra Velha Formation, Offshore Brazil, vol. 435 Geological Society, London, Special Publication.

Tosca, N.J., Wright, V.P., 2018. Diagenetic pathways linked to labile Mg-clays in lacustrine carbonate reservoirs: a model for the origin of secondary porosity in the cretaceous pre-salt Barra Velha Formation, offshore Brazil. Geol. Soc. Lond. Spec. Publ. 435, 33–46.

Tritlla, J., Loma, R., Esteban, M., Sanders, C., Sánchez, V., Benito, V., Carrasco, A., Peña, J.L., Herra, A., Gerona, M., Levresse, G. 2018. Pre-Salt Lacustrine Carbonates, Diagenetic Silicification and Hydrothermal Overprinting in Kwanza Basin (Offshore Angola): A Tale of Two Silicas. Conference Paper, AAPG ACE, Salt Lake City, Utah, USA.

Vieira de Luca, P.H., Matias, H., Carballo, J., Sineva, D., Pimentel, G.A., Tritlla, J., Esteban, M., Loma, R., Alonso, J.L.A., Jiménez, R.P., Pontet, M., Martinez, P.B., Vega, V., 2017. Breaking barriers and paradigms in presalt exploration: The Pão de Açúcar discovery (offshore Brazil). In: Merrill, R.K., Sternbach C.A. (Eds.), Giant Fields of the Decade 2000–2010. American Association of Petroleum Geologists, USA, Memoir 113, pp. 177–194.

Whitaker, F., Frazer, M. A., 2018. Process based Modelling of Syn depositional Diagenesis. In Y. Xiao, F. Whitaker, & T. Xu (Eds.), Reactive Transport Modelling: Application to subsurface energy and environmental problems (1st ed., pp. 107-156). Wiley.

Winter, W.R., Jahnert, R.J., França, A.B., 2007. Bacia de Campos. Boletim de Geociências da Petrobras 15, 511–529.

Wright, V.P., 2012. Lacustrine carbonates in rift settings: the interaction of volcanic and microbial processes on carbonate deposition. In: Garland, J., Neilson, J.E., Laubach, S., Whidden, K.J. (Eds.), Advances in Carbonate Exploration and Reservoir Analysis. Geological Society of London, Special Publications 370, pp. 39‑47.

Wright, 2022. The mantle, $CO_2$ and the giant Aptian chemogenic lacustrine carbonate factory of the South Atlantic: Some carbonates are made, not born. Sedimentology 69, 47–73.

Wright, V.P., Barnett, A.J., 2015. An abiotic model for the development of textures in some South Atlantic Early Cretaceous lacustrine carbonates, in Grotzinger, J.P., and James, N., eds., Microbial Carbonates in Space and Time: Implications for Global Exploration and Production: The Geological Society of London, Special Publication 418, p. 209–219.

Wright, V.P., Tosca, N.J., 2016. Geochemical model for the formation of the pre-salt reservoirs, Santos basin, Brazil: implications for understanding reservoir distribution. In: American Association of Petroleum Geologists Annual Convention and Exhibition, Calgary, Alberta, Canada.

Wright, V.P. and Barnett, A.J., 2017. Critically evaluating the current depositional models for the pre-salt Barra Velha Formation, Offshore Brazil. AAPG Search and Discovery, Article #51439.

Wright, V.P., Barnett, A.J., 2020. The textural evolution and ghost matrices of the Cretaceous Barra Velha Formation carbonates from the Santos Basin, offshore Brazil. Facies 66, 7.

Young, R.A. 1993. Introduction to the Rietveld Method. In: Young, R.A. (ed.) The Rietveld Method. International Union of Crystallography, Oxford University Press, p.1-38.

Ysaccis, R., El-Toukhy, M., and Moreira, L., 2019, Maximizing the value of seismic data for a better regional understanding and exploration assessment in the Santos Basin, Brazil: Brazilian Geophysical Society, 16th International Congress, Proceedings, p. 1–6.

## 8 Figures captions

Figure 1 – A) Location of the Santos Basin in the southeast region of the Brazilian continental margin. B) Location of the study area in the middle of the outer high in the Santos Basin (modified from Papaterra, 2010 and Ysaccis et al., 2019). C) Structural map of the top of the Barra Velha Formation (base of the evaporitic section), showing the location of the wells (colored dots) in the study area. The colors refer to the four paleogeographic sectors distinguished in the study area: blue wells located in the lower part of the depositional profile, green wells located in the transitional area, orange wells located in the western part of the structural high, and pink wells located in the southeastern flank of the high. The dashed line represents the approximate location of the interpreted seismic line (D). D) Interpreted seismic section of the study area, southward to transect B, oriented perpendicularly to the topographic high and showing the different tectono-stratigraphic formations of the Santos Basin (modified from Artagão, 2018).

Figure 2 – Lower Cretaceous stratigraphic chart of the Santos Basin, Brazil (modified from Moreira et al., 2007).

Figure 3 – Photomicrographs highlighting main facies of the Barra Velha Formation: (A) Fascicular calcite crusts (crossed-polarized light; XPL); (B) Mg-clay matrix engulfed by shrubs (yellow arrow). Note the shrubs partially dissolved (red arrow) (plane-polarized light; PPL);65; (C) Mg-claystones with spherulites, showing coalesced and recrystallized spherulites (PPL); (D) Mg-claystones with spherulites

showing a displacement aspect of the Mg-clay (red arrow) (XPL); (E) Mg-claystone with very fine dolomite crystals (green arrow) and dolomite rhombs (red arrows). Note the absence of spherulites in this sub-facies (PPL); (F) Laminites composed by microcrystalline calcite. Red arrows highlight dissolution seams (PPL); (G) Laminites with a crenulated morphology, composed by intercalations of very fine calcite crystals, dolomite, and organic matter. Red arrows highlight millimeter-scale silica nodules (XPL); (H) General aspects of organic matter remnants (PPL); (I) General aspects of breccia features in laminites. Red arrows highlight the intraclasts (XPL); (J) Intraclastic grainstone (Type-A) composed by fragments of fascicular calcite crusts and spherulites (PPL); (K) Type-B grainstone with volcanoclastic fragments (red arrow) (PPL); (L) Type-C grainstone (packstone) composed of carbonate and Mg-clay intraclasts (red arrows), with a minor fraction of siliciclastic grains (PPL).

Figure 4 – Facies spatial and stratigraphic distribution over the three transects (A to C, located on the map of the study area) and the three stratigraphic units labeled 3 (base) to 1 (top). No interpretation was proposed for Unit 3 of transect C, as this unit pinches out on the basement. The scale of these transects is given on the map. LMC= crenulated laminites, GST (A)= intraclastic grainstones, GST (B) intraclastic grainstone with siliciclastic/volcanoclastic content, SHR= fascicular calcite crusts, LMT= laminites, SPH= Mg-claystones with higher spherulites content, GST (C) intraclastic grainstones with Mg-clay content, MGC= Mg-claystones with lower spherulites content.

Figure 5 – Boxplots showing the diversity and amounts of accessory minerals encountered in the Barra Velha Formation, based on QEMSCAN analyses. A) Proportions of trace minerals. B) Proportions of minor minerals.

Figure 6 – (A) NW-SE transect showing the spatial and stratigraphic distribution of clay minerals (XRD). The dashed line represents the Intra-Alagoas unconformity. (B) Clay mineral composition per facies (SHR= fascicular calcite crusts, GST= intraclastic grainstones, SPH= Mg-claystones with high spherulite content, MGC= Mg-claystones with low spherulite content, LAM= laminites). The black rectangle on

1456 the last diagram is a reading example: for the samples identified as laminites facies, 33 % do not
1457 present kerolite, and 67 % present between 1-10 % of kerolite.

1458 Figure 7 – Photomicrographs highlighting different dolomite types of Barra Velha Formation: (A)
1459 Lamellar aggregates. The red arrow highlights dolomite rhombs (plane-polarized light; PPL); (B) Very
1460 fine dolomite crystals replacing calcite spherulites and possibly matrix (crossed-polarized light; XPL).
1461 Note the spherulite partially replaced by quartz (red arrow); (C) Rhombohedral dolomite replacing Mg-
1462 clay (PPL); (D) Fascicular calcite crusts with rhombohedral dolomite cement (XPL); (E) In-situ facies with
1463 anhedral dolomite cement. The red arrows highlight the carbonate constituents replaced by dolomite
1464 (PPL); (F) Grainstone with medium to coarse granular mosaic dolomite (indistinct cement and
1465 replacement phase) (PPL); (G) Grainstone with fine granular dolomite cement (PPL); (H) Fascicular
1466 calcite crusts intensely replaced by dolomite and quartz. The red arrows highlight the filling of the
1467 pore-fracture by dolomite and quartz (XPL); (I) In-situ facies with saddle dolomite. Note the sweeping
1468 extinction (red arrow; XPL).

1469 Figure 8 - (A) Mg-clay partially replaced by very fine calcite and dolomite crystals (crossed-polarized
1470 light, XPL); (B) Grainstone constituents with calcite rims. Note the dissolution of the carbonate
1471 intraclasts (plane-polarized light, PPL); (C) Grainstone with fragments of shrubs, spherulites, showing
1472 silica rims and Mg-clay envelops (red arrow). The yellow arrow highlights mosaic calcite filling porosity,
1473 the green arrow highlights calcite coating around grains (XPL); (D) Grainstone with blocky calcite
1474 cement (PPL); (E) Poikilotopic calcite, filling fracture (XPL), partially replaced by chalcedony (red arrow);
1475 (F) In-situ facies with blocky calcite engulfing saddle dolomite cement (PPL); (G) In-situ facies with
1476 intense silicification (XPL); (H) Fascicular calcite crust with quartz cement. Note the quartz replacing
1477 the fascicular calcite (red arrows); (I) Grainstone with silica rims (red arrow) and macrocrystalline
1478 quartz cement (XPL).

1479 Figure 9 – (A) Grainstone with coarse mosaic calcite, replaced by chalcedony (crossed polarized light;
1480 XPL); (B) In-situ facies with cement of dawsonite and euhedral dolomite (plane-polarized light, PPL);

(C) Cement of dawsonite and euhedral dolomite (PPL); (D) Growth-framework porosity enlarged by dissolution (PPL); (E) General aspects of dissolution in laminites; (F) General aspects of dissolution on Mg-claystones with spherulites (PPL).

Figure 10 – NW-SE correlation along transect A showing the quantitative distribution of the main diagenetic minerals in the study area. A) Boxplots of calcite, dolomite, and quartz pore-filling cement proportions. B) Vertical distribution of Mg-clay, diagenetic minerals (sum of the replacement and cementation) and dissolution. Values vary between 0 and 80% per sample for the Mg-clay and diagenetic minerals and between 0 and 60% for the dissolution process. The gamma ray log (GR) is also plotted. The profile morphology was reconstructed based on the BVF basal boundary assessed from seismic interpretation (Artagão, 2018), corroborated with the well data that reach the BVF boundary.

Figure 11 – NW-SE correlation along transect B showing the quantitative distribution of the main diagenetic minerals in the study area. A) Boxplots of calcite, dolomite, and quartz pore-filling cement proportions. B) Vertical distribution of Mg-clay, diagenetic minerals (sum of the replacement and cementation) and dissolution. Values vary between 0 and 80% per sample for the Mg-clay and diagenetic minerals and between 0 and 60% for the dissolution process. The gamma ray log (GR) is also plotted. The profile morphology was reconstructed based on the BVF basal boundary assessed from seismic interpretation (Artagão, 2018), corroborated with the well data that reach the BVF basal boundary.

Figure 12 – NW-SE correlation along transect C showing the quantitative distribution of the main diagenetic minerals in the study area. A) Boxplots of calcite, dolomite, and quartz pore-filling cement proportions. B) Vertical distribution of Mg-clay, diagenetic minerals (sum of the replacement and cementation) and dissolution. Values vary between 0 and 80% per sample for the Mg-clay and diagenetic minerals and between 0 and 60% for the dissolution process. The gamma ray log (GR) is also plotted. The profile morphology was reconstructed based on the BVF boundary assessed from seismic interpretation (Artagão, 2018), corroborated with the well data that reach the BVF boundary.

1506 Figure 13 – Scheme showing the lateral and vertical distribution of the main diagenetic phases in the
1507 study area. Purple line represents the Intra-Alagoas unconformity (between Unit 3 and 2) and the blue
1508 line represents the boundary between Units 2 and 1.

1509 Figure 14 – Boxplots showing the distribution of the different types of dolomite, in different parts of
1510 the study area and stratigraphic units. No data was collected for Unit 3 in the higher area, as it pinches
1511 out. The data of Unit 3 in the flank region are from well W11.

1512 Figure 15 - $\delta^{18}O$ vs. $\delta^{13}C$ crossplots. (A) Bulk values per facies; (B) Bulk values per stratigraphic units; (C)
1513 Samples dominated by calcite; (D) Samples dominated by dolomite. For (C) and (D), points correspond
1514 to the average values of $\delta^{18}O$ and $\delta^{13}C$ for the different facies and stratigraphic units. The horizontal
1515 and vertical bars correspond to the first and third quartile of each dataset (when available). SPH= Mg-
1516 claystones with higher spherulite content, MGC= Mg-claystones with lower spherulites content, LAM=
1517 laminites, SHR= fascicular calcite crusts, GST= grainstones of different types (A, B, C).

1518 Figure 16 – Schematic transect showing profiles of bulk mineralogy, $\delta^{13}C$, $\delta^{18}O$ of the wells W4 and W5.
1519 The well W5 does not have sufficient mineralogy data for correlation.

1520 Table 1 – Statistical summary of the average and maximum amounts of major constituents, Mg-clay
1521 and secondary porosity, in the main facies of the Barra Velha Formation. GST= intraclastic grainstones,
1522 SHR= fascicular calcite crusts, SPH= Mg-claystones with higher spherulites content, MGC= Mg-
1523 claystones with lower spherulites content, LAM= laminites.

1524 Table 2 – Statistical summary of the average and maximum amounts of major diagenetic constituents,
1525 Mg-clay, and secondary porosity, in the stratigraphic units of Barra Velha Formation.

1526 Table 3- Statistical summary of the average and maximum amounts of major diagenetic constituents,
1527 Mg-clay, and secondary porosity of Barra Velha Formation, in different portions of the study area.

Table 4 - $\delta^{18}O$ and $\delta^{13}C$ (Avg.=average value, Q1=first quartile, Q3=third quartile) for each facies and stratigraphic units (when available), for samples dominated by calcite and dolomite. Correlation coefficients are calculated for each series when number of samples (n) are sufficient.

Table 5 – Statistical summary of the average and maximum amounts of Mg-clay, dolomite, and secondary dissolution porosity in the Mg-claystones with spherulites.